Inorganic Chemistry
Forum Article

Inorg. Chem. **2010**, *49*, 3629–3645 **3629**
DOI: 10.1021/ic9020993

Heme−Copper−Dioxygen Complexes: Toward Understanding Ligand-Environmental Effects on the Coordination Geometry, Electronic Structure, and Reactivity

Zakaria Halime,[†] Matthew T. Kieber-Emmons,[‡] Munzarin F. Qayyum,[‡] Biplab Mondal,[†] Thirumanavelan Gandhi,[†] Simona C. Puiu,[†] Eduardo E. Chufán,[†] Amy A. N. Sarjeant,[†] Keith O. Hodgson,[‡,§] Britt Hedman,[§] Edward I. Solomon,[*,‡,§] and Kenneth D. Karlin[*,†,⊥]

[†]*Department of Chemistry, The Johns Hopkins University, Baltimore, Maryland 21218,* [⊥]*Department of Bioinspired Science, Ewha Woman's University, Seoul 120-750, Korea,* [‡]*Department of Chemistry, Stanford University, Stanford, California 94305, and* [§]*Stanford Synchrotron Radiation Lightsource, SLAC, Stanford University, Stanford, California 94309*

Received October 23, 2009

The nature of the ligand is an important aspect of controlling the structure and reactivity in coordination chemistry. In connection with our study of heme−copper−oxygen reactivity relevant to cytochrome *c* oxidase dioxygen-reduction chemistry, we compare the molecular and electronic structures of two high-spin heme−peroxo−copper $[Fe^{III}O_2^{2-}Cu^{II}]^+$ complexes containing N_4 tetradentate (**1**) or N_3 tridentate (**2**) copper ligands. Combining previously reported and new resonance Raman and EXAFS data coupled to density functional theory calculations, we report a geometric structure and more complete electronic description of the high-spin heme−peroxo−copper complexes **1** and **2**, which establish μ-(O_2^{2-}) side-on to the Fe^{III} and end-on to Cu^{II} (μ-η^2:η^1) binding for the complex **1** but side-on/side-on (μ-η^2:η^2) μ-peroxo coordination for the complex **2**. We also compare and summarize the differences and similarities of these two complexes in their reactivity toward CO, PPh_3, acid, and phenols. The comparison of a new X-ray structure of μ-oxo complex **2a** with the previously reported **1a** X-ray structure, two thermal decomposition products respectively of **2** and **1**, reveals a considerable difference in the Fe−O−Cu angle between the two μ-oxo complexes ($\angle$Fe−O−Cu = 178.2° in **1a** and $\angle$Fe−O−Cu = 149.5° in **2a**). The reaction of **2** with 1 equiv of an exogenous nitrogen-donor axial base leads to the formation of a distinctive low-temperature-stable, low-spin heme−dioxygen−copper complex (**2b**), but under the same conditions, the addition of an axial base to **1** leads to the dissociation of the heme−peroxo−copper assembly and the release of O_2. **2b** reacts with phenols performing H-atom ($e^- + H^+$) abstraction resulting in O−O bond cleavage and the formation of high-valent ferryl $[Fe^{IV}=O]$ complex (**2c**). The nature of **2c** was confirmed by a comparison of its spectroscopic features and reactivity with those of an independently prepared ferryl complex. The phenoxyl radical generated by the H-atom abstraction was either (1) directly detected by electron paramagnetic resonance spectroscopy using phenols that produce stable radicals or (2) indirectly detected by the coupling product of two phenoxyl radicals.

Introduction

In the past few years, we have been engaged in heme−copper (Cu)−dioxygen (O_2) reactivity studies using synthetic systems, with the goal being to provide fundamental information of possible relevance to biological heme−copper oxidases (HCOs), which include cytochrome *c* oxidase (C*c*O). HCOs are the terminal enzymes of the respiratory chain that catalyze the reduction of molecular oxygen to water, a process that requires four electrons and four protons:

$$O_2 + 4e^- \text{ (from cyt-c}_{\text{reduced}}) + 8H^+ \text{ (from inside the membrane)} \rightarrow 2H_2O + 4H^+ \text{ (membrane translocated)} + 4\text{cyt-c}_{\text{oxidized}}$$

The reaction is coupled to the pumping of four additional protons across the mitochondrial or bacterial membrane, which ultimately is utilized to drive ATP synthetase activity and thus generate ATP, which is stored and used in subsequent metabolic functions.[1−6]

*To whom correspondence should be addressed. E-mail: karlin@jhu.edu (K.D.K.), edward.solomon@stanford.edu (E.I.S.).

(1) Ferguson-Miller, S.; Babcock, G. T. *Chem. Rev.* **1996**, *96*, 2889–2907.
(2) Iwata, S.; Ostermeier, C.; Ludwig, B.; Michel, H. *Nature* **1995**, *376*, 660–669.
(3) Yoshikawa, S.; Shinzawa-Itoh, K.; Nakashima, R.; Yaono, R.; Yamashita, E.; Inoue, N.; Yao, M.; Jei-Fei, M.; Libeu, C. P.; Mizushima, T.; Yamaguchi, H.; Tomizaki, T.; Tsukihara, T. *Science* **1998**, *280*, 1723–1729.
(4) Kim, E.; Chufán, E. E.; Kamaraj, K.; Karlin, K. D. *Chem. Rev.* **2004**, *104*, 1077–1133.
(5) Collman, J. P.; Boulatov, R.; Sunderland, C. J.; Fu, L. *Chem. Rev.* **2004**, *104*, 561–588.
(6) Chufán, E. E.; Puiu, S. C.; Karlin, K. D. *Acc. Chem. Res.* **2007**, *40*, 563–572.

Published on Web 04/12/2010

Scheme 1

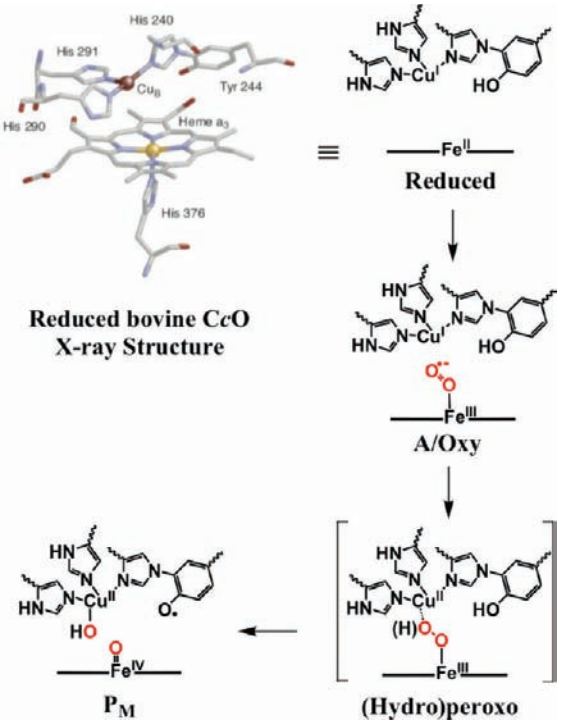

In the heme−Cu active-site-mediated O_2 reduction by HCOs, O_2 reacts with a fully reduced $Fe^{II}\cdots Cu^{I}$ binuclear center (Scheme 1), initially forming a detectable transient, the $Fe^{III}(O_2^{-})\cdots Cu^{I}$ complex **A**. **A** exhibits UV−vis and resonance Raman (rR) spectroscopic properties very similar to those known for oxy hemoglobin or myoglobin. A density functional theory (DFT)-calculated structure of **A** supports the $Fe^{III}(O_2^{-})\cdots Cu^{I}$ formulation with the Cu ion positioned very close to the superoxo O atom, $Cu\cdots O = 2.12$ Å.[7] The next transformation seems optimized to prevent leakage of deleterious intermediates such as a hydroxyl radical or hydrogen peroxide, wherein rapid overall four-electron reductive O−O cleavage is completed, giving $\mathbf{P_M}$, in which a closeby coupled Tyr (Scheme 1) or nearby Trp[8] residue efficiently provides a needed electron. A peroxo-bridged $Fe^{III}(O_2^{2-})Cu^{II}$ transient has been discussed as possibly forming from **A** prior to $\mathbf{P_M}$ formation.[9−12] Also discussed and calculated is an electron transfer from Cu_B^{I} in **A**, which is accompanied by H^+ uptake to give a μ-hydroperoxo transient, $Fe_{a_3}^{III}OO(H)Cu_B^{II}$; the protonation event in this scenario would trigger electron transfer (from the heme a_3 and the Tyr244), yielding a cleaved O−O product ferryl moiety (state $\mathbf{P_M}$; Scheme 1).[10,13−15]

Synthetic modeling presents a chemically interesting, if not necessary, approach to studying the metalloprotein active site structure (electronic and connectivity) and reactivity and its relationship with the inherent fundamental chemistry associated with the metal ion and its ligand environment.[16−18] Of particular interest is the **A** to $\mathbf{P_M}$ conversion because O−O cleavage chemistry is of broad fundamental and practical importance in the utilization of molecular oxygen such as in biological "O_2 activation" occurring in heme, nonheme iron and copper oxidases, or oxygenases. The use of O_2 (from air) in practical (chemical/industrial) organic oxidations, or energy production in fuel cell technologies, also involves O−O cleavage. The reverse process, O−O bond formation, occcurs in photosynthesis and is of great contemporary interest and importance as related to worldwide energy concerns. This timely Forum highlights the importance of understanding the elementary kinetic steps required to reductively cleave the O−O bond and the many ways in which researchers are tackling such issues.

In this Forum Article, we will highlight our own studies in the synthetic modeling of heme−copper oxidases, also providing new insights obtained on the heme−Cu−O_2 adduct structure, bonding, and reactivity. In our earlier studies, we have employed a systematic approach varying the design of heme−Cu complexes.[6] The approach entails synthetic modulation of the Cu ligand type, denticity, arrangement of donors, heme axial "base" ligand, and availability of protons or reducing equivalents. The overarching question is how such factors influence heme−Cu−O_2-derived structures, along with the resulting complex Fe−O_2(H)-bonding and electronic structure (i.e., spin state, level of reduction of O_2, etc.). Such *factors* have been shown or are expected to dictate the absence or presence of further reactivity and the nature of such reactivity in the context of O−O cleavage chemistry. With similar emphases, in part, the research groups of Collman and co-workers[5,19] and Naruta and co-workers[20,21] have been very active and have made major contributions. Collman has also presented a longtime program in biomimetic electrode surface electrocatalysis of the four-electron O_2 reduction to water.[5,22,23] Despite many achievements and advancements from all groups, there remains a considerable lack of detail concerning the structure of heme−Cu−O2-derived adducts, and therefore we do not have firm correlations between the structure bonding and ensuing reactivity. The latter involves protonation and electron-transfer steps, for which a deeper understanding of the thermodynamics and timing or order is required.

In our initial attempts to mimic the O_2-reduction chemistry of C*c*O, we utilized TMPA-Cu^{I} complexes, where tris(2-pyridylmethylamine) (TMPA) is a tetradentate N_4 ligand.

(7) Blomberg, L. M.; Blomberg, M. R. A.; Siegbahn, P. E. M. *J. Inorg. Biochem.* **2005**, *99*, 949–958.
(8) de Vries, S. *Biochimica et Biophysica Acta* (*BBA*) - *Bioenergetics* **2008**, *1777*, 925–928.
(9) Proshlyakov, D. A.; Pressler, M. A.; Babcock, G. T. *Proc. Natl. Acad. Sci. U.S.A.* **1998**, *95*, 8020–8025.
(10) Blomberg, M. R. A.; Siegbahn, P. E. M.; Wikström, M. *Inorg, Chem.* **2003**, *42*, 5231–5243.
(11) Ogura, T.; Kitagawa, T. *Biochim. Biophys. Acta* **2004**, *1655*, 290–297.
(12) Blomberg, M. R. A.; Siegbahn, P. E. M. *Biochim. Biophys. Acta* **2006**, *1757*, 969–980.
(13) Himo, F.; Siegbahn, P. E. M. *Chem. Rev.* **2003**, *103*, 2421–2456.
(14) Huynh, M. H. V.; Meyer, T. *J. Chem. Rev.* **2007**, *107*, 5004–5064.
(15) Yoshioka, Y.; Satoh, H.; Mitani, M. *J. Inorg. Biochem.* **2007**, *101*, 1410–1427.
(16) Karlin, K. D. *Science* **1993**, *261*, 701–708.
(17) Holm, R. H.; Solomon, E. I.; Editors "Biomimetic Inorganic Chemistry," In *Chem. Rev.* **2004**; Vol. *104* (2).
(18) Lee, Y.; Karlin, K. D. "Highlights of Copper Protein Active-Site Structure/Reactivity and Synthetic Model Studies," In *Concepts and Models in Bioinorganic Chemistry*; N. Metzler-Nolte Kraatz, H.-B., Ed.; Wiley-VCH: New York, 2006; pp 363−395.
(19) Collman, J. P.; Decréau, R. A. *Chem. Commun.* **2008**, 5065–5076.
(20) Liu, J. G.; Naruta, Y.; Tani, F. *Angew. Chem., Int. Ed.* **2005**, *44*, 1836–1840.
(21) Liu, J.-G.; Naruta, Y.; Tani, F. *Chem.—Eur. J.* **2007**, *13*, 6365–6378.
(22) Collman, J. P.; Devaraj, N. K.; Decreau, R. A.; Yang, Y.; Yan, Y.-L.; Ebina, W.; Eberspacher, T. A.; Chidsey, C. E. D. *Science* **2007**, *315*, 1565–1568.
(23) Bröring, M. *Angew. Chem., Int. Ed.* **2007**, *46*, 6222–6224.

Chart 1

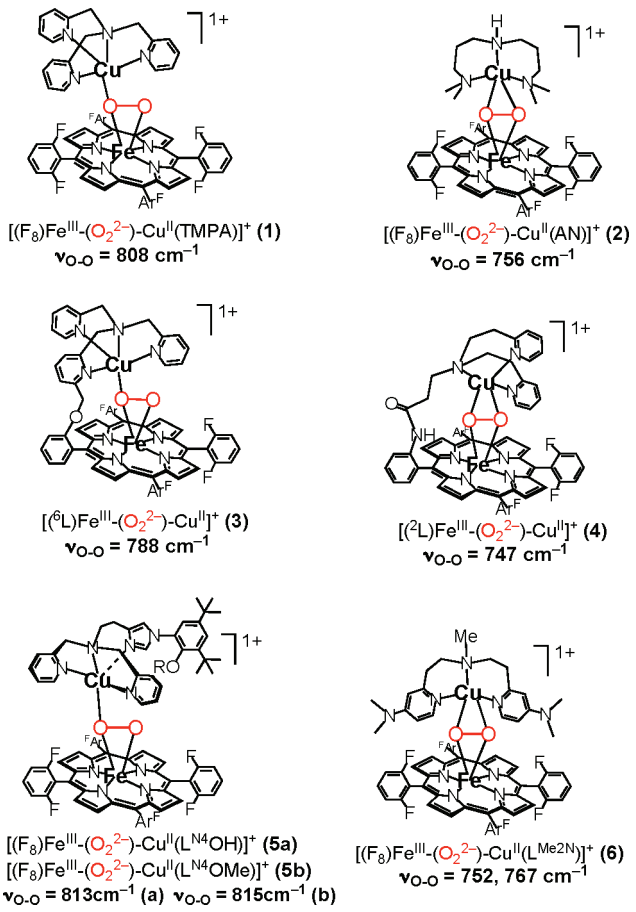

We observed that a low-temperature-stable heme-Fe^{III}−peroxo−Cu^{II} complex $[(F_8)Fe^{III}(O_2^{2-})Cu^{II}(TMPA)]^+$ (**1**; Chart 1) could be generated from the O_2 reaction with an equimolar mixture of $(F_8)Fe^{II}$ and $[Cu^{I}(TMPA)]^+$ (see the discussion below), where F_8 = tetrakis(2,6-difluorophenyl)-porphyrinate^{2-}.[24] Structural investigation of the ensuing complex using rR and X-ray absorption (XANES and EXAFS) spectroscopies coupled to DFT calculations indicated that the peroxide unit is bound side-on to the high-spin (HS) iron(III) (overall hexacoordinate with the iron out of the porphyrinate plane) and end-on to the copper(II) (overall penta-coordinate), thus an Fe^{III}−(μ-η^2:η^1-peroxo)−Cu^{II} coordination mode.[25,26] An intraperoxide stretching band was observed in the rR spectrum at 808 cm^{-1}.[24,25] The plausibility of such a coordination mode was affirmed by Naruta and co-workers, through crystallographic characterization of such a complex possessing a closely related ligand framework.[27] There, ν_{O-O} was determined to be 790 cm^{-1} (Figure 1).

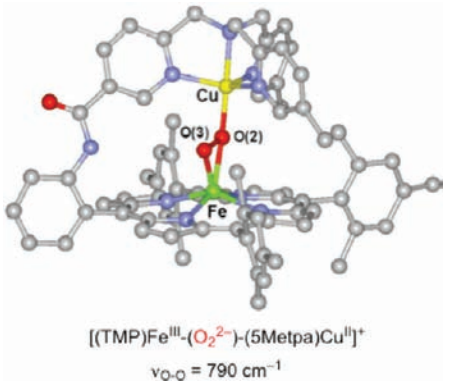

Figure 1. X-ray structure of $[(TMP)Fe^{III}(O_2^{2-})(5Metpa)Cu^{II}]^+$ synthesized and characterized by Naruta and co-workers.

We also established the same μ-η^2:η^1 coordination mode in three other peroxo complexes containing tetradenate Cu ligands (Chart 1). In $[(^6L)Fe^{III}(O_2^{2-})Cu^{II}]^+$ (**3**), the tetradentate TMPA ligand is covalently appended to the periphery of a 2,6-difluorophenyl-substituted porphyrin and ν_{O-O} = 788 cm^{-1}.[28,29] In $[(F_8)Fe^{III}(O_2^{2-})Cu^{II}(L^{N4OH})]^+$ (**5a**) and $[(F_8)Fe^{III}(O_2^{2-})Cu^{II}(L^{N4OMe})]^+$ (**5b**), the Cu ligand is a modified version of TMPA, where one pyridine is replaced by a protected (**5b**) or nonprotected (**5a**) imidazole−phenol moiety to mimic the cross-linked histidine−tyrosine in the C*c*O active site. The O−O stretching frequencies in **5a** and **5b** are 813 and 815 cm^{-1}, respectively.[6,30] Extensive previous (and ongoing) Cu^{I}−O_2 chemical investigations have shown that even subtle differences in the ligand/denticity can dramatically change the nature of the Cu−O_2 adduct and its reactivity toward substrates.[31,32] Tetradentate ligands, such as TMPA, induce the formation of end-on (μ-1,2) peroxo−Cu^{II}_2 structures (Chart 2), whereas tridentate ligands generate side-on (μ-η^2:η^2) peroxo−Cu^{II}_2 species.[33] The former possess relatively average ν_{O-O} values, typically above 800 cm^{-1} (Chart 2). However, the latter side-on complexes have reduced ($<$760 cm^{-1}) ν_{O-O} values (Chart 2), ascribed to back-bonding from the copper-to-peroxo antibonding σ^* orbital, which considerably weakens the O−O bond.[34−36]

To compare and contrast the chemistry with that for the heme−Cu system possessing tetradentate Cu ligands, we expanded our study to heme−Cu systems containing tridentate Cu ligands. Within that context, we reported the synthesis and characterization of three HS heme−peroxo−Cu complexes with tridentate Cu ligands (Chart 1): (1) $[(F_8)Fe^{III}(O_2^{2-})$-$Cu^{II}(AN)]^+$ (**2**) [AN = bis[3-(dimethylamino)propyl]amine],[37]

(24) Ghiladi, R. A.; Hatwell, K. R.; Karlin, K. D.; Huang, H.-w.; Moënne-Loccoz, P.; Krebs, C.; Huynh, B. H.; Marzilli, L. A.; Cotter, R. J.; Kaderli, S.; Zuberbühler, A. D. *J. Am. Chem. Soc.* **2001**, *123*, 6183–6184.
(25) del Rio, D.; Sarangi, R.; Chufán, E. E.; Karlin, K. D.; Hedman, B.; Hodgson, K. O.; Solomon, E. I. *J. Am. Chem. Soc.* **2005**, *127*, 11969–11978.
(26) Ghiladi, R. A.; Chufan, E. E.; del Rio, D.; Solomon, E. I.; Krebs, C.; Huynh, B. H.; Huang, H. w.; Moenne-Loccoz, P.; Kaderli, S.; Honecker, M.; Zuberbuhler, A. D.; Marzilli, L.; Cotter, R. J.; Karlin, K. D. *Inorg. Chem.* **2007**, *46*, 3889–3902.
(27) Chishiro, T.; Shimazaki, Y.; Tani, F.; Tachi, Y.; Naruta, Y.; Karasawa, S.; Hayami, S.; Maeda, Y. *Angew. Chem., Int. Ed.* **2003**, *42*, 2788–2791.
(28) Ghiladi, R. A.; Ju, T. D.; Lee, D.-H.; Moënne-Loccoz, P.; Kaderli, S.; Neuhold, Y.-M.; Zuberbühler, A. D.; Woods, A. S.; Cotter, R. J.; Karlin, K. D. *J. Am. Chem. Soc.* **1999**, *121*, 9885–9886.
(29) Ghiladi, R. A.; Huang, H. W.; Moënne-Loccoz, P.; Stasser, J.; Blackburn, N. J.; Woods, A. S.; Cotter, R. J.; Incarvito, C. D.; Rheingold, A. L.; Karlin, K. D. *J. Biol. Inorg. Chem.* **2005**, *10*, 63–77.
(30) Kim, E.; Kamaraj, K.; Galliker, B.; Rubie, N. D.; Moënne-Loccoz, P.; Kaderli, S.; Zuberbühler, A. D.; Karlin, K. D. *Inorg. Chem.* **2005**, *44*, 1238–1247.
(31) Hatcher, L. Q.; Karlin, K. D. *Adv. Inorg. Chem.* **2006**, *58*, 131–184.
(32) Hatcher, L. Q.; Karlin, K. D. *J. Biol. Inorg. Chem.* **2004**, *9*, 669–683.
(33) Mirica, L. M.; Ottenwaelder, X.; Stack, T. D. P. *Chem. Rev.* **2004**, *104*, 1013–1045.
(34) Ross, P. K.; Solomon, E. I. *J. Am. Chem. Soc.* **1991**, *113*, 3246–3259.
(35) Ross, P. K.; Solomon, E. I. *J. Am. Chem. Soc.* **1990**, *112*, 5871–5872.
(36) Solomon, E. I.; Tuczek, F.; Root, D. E.; Brown, C. A. *Chem. Rev.* **1994**, *94*, 827–856.
(37) Chufan, E. E.; Mondal, B.; Gandhi, T.; Kim, E.; Rubie, N. D.; Moenne-Loccoz, P.; Karlin, K. D. *Inorg. Chem.* **2007**, *46*, 6382–6394.

Chart 2

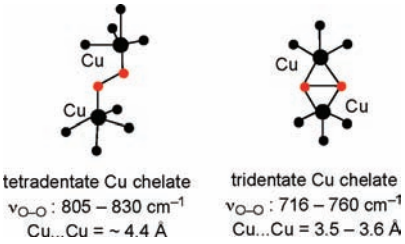

Scheme 2

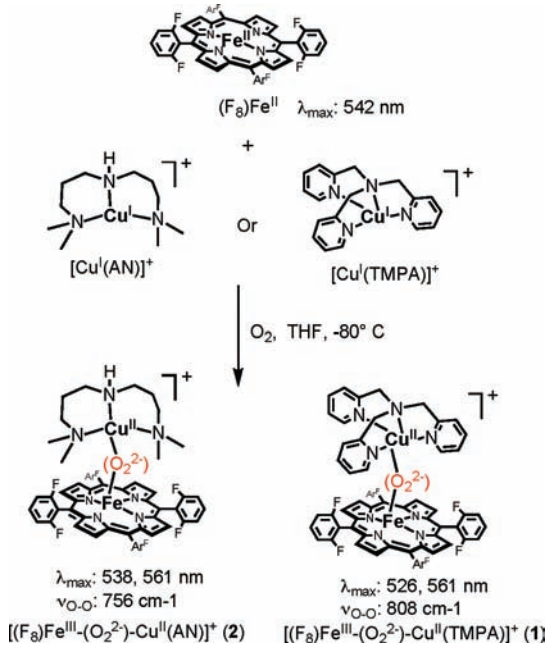

(2) $[(F_8)Fe^{III}(O_2^{2-})Cu^{II}(L^{Me_2}N)]^+$ (**6**) ($L^{Me_2}N$ = *N*,*N*-bis[2-(2-pyridyl)ethyl]methylamine),[38] and (3) $[(^2L)Fe^{III}(O_2^{2-})Cu^{II}]^+$ (**4**) (^2L = tethered prophryn-*N*,*N*-bis[2-(2-pyridyl)ethyl]methylamine).[39,40] In concordance with expectations from Cu−O_2 homodimer chemistry (Chart 2), the three complexes present O−O stretching frequencies below 760 cm^{-1}, thereby suggesting a side-on (μ-η^2:η^2) mode of coordination for the peroxo bridge. Thus, the heme−peroxo−Cu complexes depicted in Chart 1 were tentatively assigned as such.[40] In this paper, this point is addressed in detail, following new rR and EXAFS spectroscopic studies supported by DFT calculations.

Further, in this report we have selected **1** and **2** containing tetra- and tridentate Cu ligands, respectively, to compare and contrast the molecular structure, electronic structure bonding, and resultant reactivity, combining some previously published information, along with new data. The overall goal is to contribute a better understanding of the relationship between the denticity of the Cu ligand to the structure and reactivity of HS heme−peroxo−Cu complexes. We also describe the formation and initial characterization of a new related low-spin (LS) heme−peroxo−Cu complex and compare the HS and LS complexes in their reactivity toward phenols as H-atom ($H^+ + e^-$) donors.

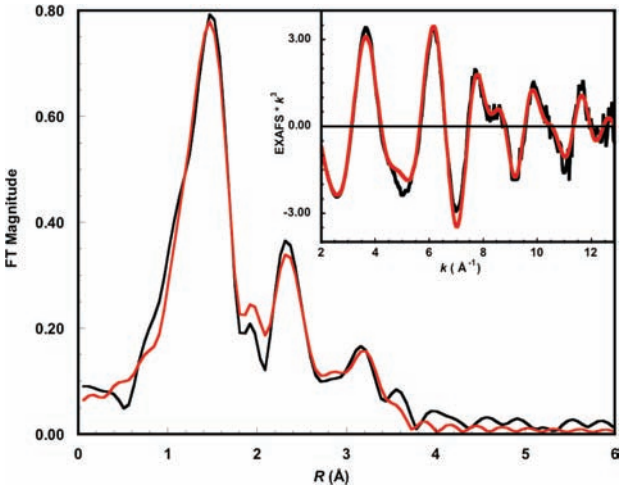

Figure 2. Cu K-edge EXAFS data to k = 12.8 Å^{-1} (inset) and a non-phase-shift-corrected FT of the EXAFS data for **2** in solution: data (black); fit (red). The phase shift in the first shell is ~0.4 Å.

Results and Discussion

Generation of HS Heme−Peroxo−Cu Complexes. As mentioned, **1** has been structurally characterized, through a variety of spectroscopic studies, computational chemistry, and comparison to the Naruta complex. These possess a μ-η^2:η^1-peroxo ligation. A major goal of the present work is to elucidate or confirm the μ-η^2:η^2 side-on peroxo structure previously proposed for **4** (and thus **6**) employing **2** for such studies; the latter possesses synthetically more accessible precursor components and has been found to be more stable and amenable to spectroscopic interrogation.

As previously described, **1** and **2** can be cleanly generated by bubbling O_2 at low temperature through an equimolar solution of $(F_8)Fe^{II}$ and $[Cu^I(AN)](B(C_6F_5)_4)$ or $[Cu^I(TMPA)](B(C_6F_5)_4)$[6,37] (Scheme 2). With tridentate chelating ligands for the Cu ion, complexes **2**, **4**, and **6** possess the same UV−vis features in the Q-band region, but which are clearly distinguishable from those of **1**, **3**, and **5** with their tetradentate Cu ligands.[39] In the former case, a second prominent absorption occurs, e.g., at 538 nm for **2** (Scheme 2). Low-temperature ^{1}H NMR characterization of the μ-peroxo products **1** and **2** shows a downfield-shifted pyrrole resonance at ~95 ppm, which has been confirmed by ^{2}H NMR studies using the deuterated pyrrole $(F_8)Fe^{II}$-d_8 analogue) in the synthesis. This finding excludes the possibility that the product observed is (i) the η^2-peroxo compound $[(F_8)Fe^{III}]_2(O_2^{2-})$ (~17.5 ppm, −80 °C), (ii) an iron superoxide complex, that is, $(F_8)Fe^{III}(O_2^-)$ (~8.9 ppm, −80 °C), (iii) the ferryl species $(F_8)Fe^{IV}$=O (~3.5 ppm, −80 °C), or (iv) $(F_8)Fe^{III}$OH (~135 ppm, −80 °C).[41] In fact, the 95 ppm pyrrole

(38) Kim, E.; Helton, M. E.; Wasser, I. M.; Karlin, K. D.; Lu, S.; Huang, H.-w.; Moënne-Loccoz, P.; Incarvito, C. D.; Rheingold, A. L.; Honecker, M.; Kaderli, S.; Zuberbühler, A. D. *Proc. Natl. Acad. Sci. U.S.A.* **2003**, *100*, 3623–3628.

(39) Kim, E.; Helton, M. E.; Lu, S.; Moënne-Loccoz, P.; Incarvito, C. D.; Rheingold, A. L.; Kaderli, S.; Zuberbühler, A. D.; Karlin, K. D. *Inorg. Chem.* **2005**, *44*, 7014–7029.

(40) Kim, E.; Shearer, J.; Lu, S.; Moënne-Loccoz, P.; Helton, M. E.; Kaderli, S.; Zuberbühler, A. D.; Karlin, K. D. *J. Am. Chem. Soc.* **2004**, *126*, 12716–12717.

(41) Ghiladi, R. A.; Kretzer, R. M.; Guzei, I.; Rheingold, A. L.; Neuhold, Y.-M.; Hatwell, K. R.; Zuberbühler, A. D.; Karlin, K. D. *Inorg. Chem.* **2001**, *40*, 5754–5767.

Table 1. EXAFS Least-Squares Fitting Results for **2**

Cu						Fe					
coordn	path	R(Å)[a]	σ^2(Å^2)[b]	ΔE_0(eV)	F[c]	coordn	path	R(Å)[a]	σ^2(Å^2)[b]	ΔE_0(eV)	F[c]
5	Cu−N/O	2.00	963	−9.61	0.07	1	Fe−O/N	1.94	257	−2.09	0.23
6	Cu−C	2.92	701			5	Fe−N/O	2.09	397		
16	Cu−N−C	3.22	311			8	Fe−C	3.10	368		
1	Cu−Fe	3.62	653			16	Fe−N−C[d]	3.32	368		
2	Cu−O−Fe	3.75	809			4	Fe−C	3.49	864		
						1	Fe−Cu	3.64	370		
						2	Fe−O−Cu[d]	3.71	370		
						5	Fe−C	3.81	461		
						12	Fe−N−C	4.38	513		
						16	Fe−C−C	4.91	377		
						8	Fe−C−C	4.98	291		

[a] The estimated standard deviation in R for each fit is ±0.02 Å. [b] The σ^2 values are multiplied by 10^5. [c] The error, F, is given by $\sum[(\chi_{obsd} - \chi_{calcd})^2k^6]/\sum[(\chi_{obsd})^2k^6]$. [d] σ^2 for the MS path is linked to that of the corresponding SS path. The errors in the ΔE_0 values are ±0.22 eV for Cu and ±0.27 eV for Fe. The estimated errors in σ^2 are 5−30%. The error in the coordination number is 20−25%, and that in the identity of the scatterer Z is ±1.

resonance is in the range expected for a HS Fe^{III} (d^5, $S = {}^5/_2$) system that is strongly antiferromagnetically coupled to a Cu^{II} ion (d^9, $S = {}^1/_2$), giving an overall $S = 2$ spin system (confirmed in **1** by solution magnetic moment measurement $\mu_{eff} = 5.1\ \mu_B$ at −40 °C). Further, in the case of **1**, MALDI-TOF-MS reveals the presence of a O_2 adduct with a stoichiometry of $(F_8)Fe$: $Cu^{II}(TMPA):O_2 = 1:1:1$ ratio, and solution mass spectral data give the correct O_2-derived moiety (for which m/z increases by 4 when using $^{18}O_2$).[26]

Coordination Geometry and Electronic Structural Comparisons of 1 and 2. Cu EXAFS. The k^3-weighted Cu K-edge EXAFS spectroscopic data and Fourier transform (FT) of **2** are shown in Figure 2. The EXAFS fit parameters are given in Table 1. The first-shell EXAFS data were fit best with five Cu−O/N contributions at 2.00 Å.[42] The theoretical phase and amplitude parameters were calculated from a Cu−N path. Using a Cu−O path, the best first-shell fit resulted in a coordination number of 4. This difference in the first-shell coordination is within the estimated 20−25% error. Split first-shell fits with a combination of one to four short Cu−O/N with one to four longer Cu−N/O were also performed. These fits gave higher error with a split in the distance between the two paths of less than the resolution of the data (0.14 Å). The paths corresponding to the FT peak in the $R = 2$−2.8 Å range were fit using single-scattering (SS) and multiple-scattering (MS) contributions from the AN alkyl backbone. The FT peak in the $R = 2.8$−3.8 Å range was fit with a Cu···Fe SS contribution at 3.62 Å with its corresponding MS Cu−O−Fe vector refined to 3.75 Å when both distances and σ^2 values were allowed to float independently for these paths. Linking the σ^2 values for these paths resulted in a fit with a Cu···Fe distance of 3.63 Å and a Cu−O−Fe MS distance of 3.76 Å with a σ^2 value of 627×10^{-5} Å^2. The Cu···Fe vector distance varied between fits to the data of four different samples and with slightly different splines, giving an average Cu···Fe distance of 3.63 ± 0.04 Å.

Fe EXAFS. The k^3-weighted Fe K-edge EXAFS spectroscopic data and FT of **2** are shown in Figure 3. The first backscattering shell was fit best using one Fe−O/N contribution at 1.94 Å and five Fe−N/O contributions at 2.09 Å. The second-shell FT peak in the $R = 2$−3 Å range was fit using the porphyrin pyrrole α-C SS and MS contributions, along with the SS contribution from the *meso*-C atoms. The Fe···Cu contribution was fit at 3.64 Å with its corresponding MS Fe−O−Cu vector refined to 3.71 Å when the two σ^2 values were linked to each other. Floating the σ^2 values for these paths resulted in very similar fit parameters. The Fe···Cu vector was not required to get a good fit to the EXAFS data. This is because the SS and MS contributions from the porphyrin pyrrole β-C atoms interfere with the signal from the Fe···Cu interaction, making the metal−metal vector hard to determine. The reliable distance of the Fe···Cu interaction was thus obtained from Cu EXAFS. The intensity in the $R = 3.5$−5 Å FT range was fit with SS and MS components from the pyrrole β- and γ-C atoms.

Comparison of EXAFS between 1 and 2. The Cu K-edge EXAFS and FT of frozen solutions of **1** and **2** are compared in Figure S6 in the Supporting Information. Both species have a first-shell coordination of 5 Cu−N/O, which in the case of **1** can be split to obtain a short Cu−O/N of 1.87 Å. The two EXAFS patterns between $k = 4$ and 12 Å^{-1} are significantly different and account for the contrasting Cu ligands and Cu···Fe vectors in the two species. The slight phase shift to lower k in **1** is consistent with a lenghthened Cu···Fe vector in **1** of 3.72 Å compared to 3.63 Å in **2**. The higher EXAFS intensity in **1** is reflected in the higher FT intensity in which a major difference is observed from $R = 3$−4 Å. The signal in this region originates from the Cu···Fe interaction, which in **1** is much more intense because the Cu−O−Fe MS is stronger than that in **2**. This difference arises from the more linear Cu−O−Fe angle of 150° in **1** compared to 134° in **2**. Both angles have been calculated from EXAFS parameters.[43] The deconvoluted sine waves from the SS and MS of Cu−Fe and Cu−O−Fe, respectively, are shown in Figure S8 in the Supporting Information. A Cu−O−Fe angle of 150° is not enough to produce such an intense MS wave in **1**. Some of the intensity in the $R = 3$−4 Å region is a result of SS and MS contributions from the light atoms of TMPA. The remainder of the difference

(42) The EXAFS envelopes obtained from a single scatterer (SS) with atomic number Z and $Z \pm 1$ at the same distance from the absorber are indistinguishable. Thus, Cu-O/N refers to a SS contribution from either O or N.

(43) $\angle$Cu-O-Fe = $\cos^{-1}\{[(Cu\text{-}O)^2+(Fe\text{-}O)^2-(Cu\text{-}Fe)^2]/2(Cu\text{-}O)(Fe\text{-}O)\}$.

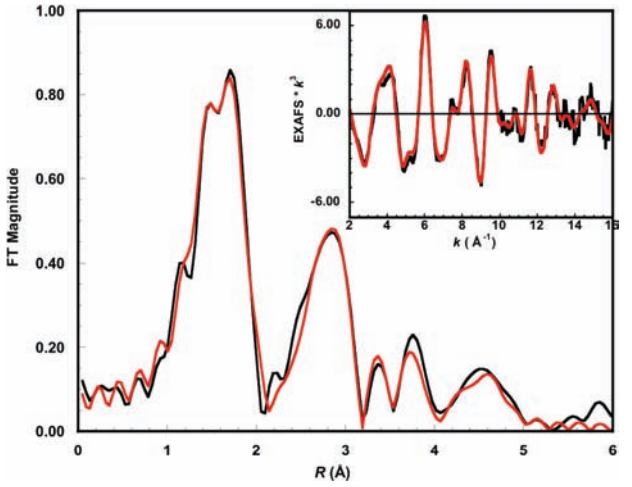

Figure 3. Fe K-edge EXAFS data to $k = 16$ Å^{-1} (inset) and a non-phase-shift-corrected FT of $[(F_8)Fe^{III}O_2Cu^{II}(AN)](ClO_4)$ in solution form: data (black); fit (red). The phase shift in the first shell is ~0.4 Å.

between $R = 2.5$ and 5 Å is due to the different SS and MS contributions from the pyridine versus alkylamine side chains.

The Fe K-edge EXAFS and FT of the solution data of **1** and **2** are compared in Figure S7 in the Supporting Information. Both have a split first shell with a short Fe−O/N at 1.92 and 1.94 Å, respectively, and 5 Fe−N/O at 2.09 Å. The small changes in the first-shell FT are possibly from the different interferences of the two sine waves in each system. The EXAFS beat patterns are very similar in both species. The higher intensity in **1** is again from the stronger Fe−O−Cu MS. This higher intensity translates into the FT peak at 3.5 Å in **1** that is missing in **2**. Both **1** and **2** have very similar coordination environments around Fe, as seen from the Fe EXAFS. The Fe K-edge and pre-edge (Figure S9 in the Supporting Information) lend further support to the Fe being in a very similar coordination environment. The pre-edge peak intensity at ~7113.5 eV is a result of a 1s → 3d transition that is dipole-forbidden but quadrupole-allowed. This peak gains intensity from 4p mixing into the 3d ground state. Distortion away from centrosymmetry increases 4p−3d mixing as the Fe is pulled out of the heme plane. The similar pre-edge peak intensities in the two systems suggest that the peroxo binding to Fe is similar in both species, i.e., side-on, as a consequence of similar Fe coordination.

rR Spectroscopy. The O−O stretching frequencies of both **1** and **2** have been previously reported as 810 and 756 cm^{-1}, respectively,[24,37] indicating the peroxo character of the bound O_2 moiety. However, the significant difference between these two energies was hypothesized as being due to a distinct core geometry, namely, μ-η^2:η^2 for **2** relative to μ-η^2:η^1 found in **1**. To evaluate this possibility and an alternative η^1 coordination mode at the Fe, rR spectroscopy was performed to assess the displacement of the iron out of the heme pocket. In particular, the energy of the oxidation and spin-state-sensitive marker band ν_4 was recorded. From the spectra in Figure 4, the ν_4 band of **2** is observed at 1362 cm^{-1},

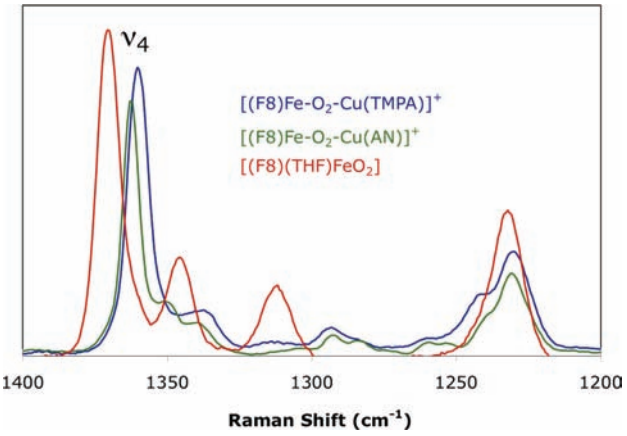

Figure 4. rR spectra with 413 nm excitation of **1** (blue), **2** (green), and $[(F_8)(THF)FeO_2]$ (red).

which compares well with that of **1** (1360 cm^{-1}). A bona fide end-on O_2-bound heme, $[(F_8)(THF)Fe(O_2)]$,[24,26,38,44] with the Fe in the porphryn plane was measured as a control and exhibits a ν_4 of 1370 cm^{-1}.

Geometric Structures. Spin-unrestricted DFT calculations were performed using the BP86 functional on **1** and **2**. The optimized structures are shown in Figure 5, and selected bond angles and distances are reported in Table 2. An optimized structure of a truncated model lacking phenyl rings of the heme of **1** was previously reported;[25,26] however, the full structure of **1** was reoptimized herein to facilitate structural comparisons between **1** and **2**. The metrical parameters of the μ-η^2:η^1 Fe−O_2−Cu core in the present structure of **1** agree well with the previously reported metrical parameters of the truncated model, and this indicates that the heme phenyl substituents exhibit only a minor effect on the core. The core structure of **1** is likewise very analogous to that of the crystallographically characterized tethered complex of Naruta and co-workers,[27] $\{[(TMP)Fe]O_2[Cu(5MeTPA)]\}^+$. Both molecules display a degree of ruffling of the porphyrin macrocycles, a feature not observed in the previous calculations of **1**, presumably because of their lack of phenyl substituents. The ruffling causes the four coordinating N atoms to deviate slightly from planarity. Thus, displacement of the Fe out of the heme pseudoplane (0.56 Å in the case of **2**) is reported as an average displacement.

In contrast to the μ-η^2:η^1 structure of **1**, the geometry-optimized core structure of **2** displays the peroxo moiety spanning the metals in a μ-η^2:η^2 configuration, where the peroxo ligand has gone from η^1 to η^2 on Cu in going from **1** to **2**. This is the first example of such a coordination in heme−peroxo−Cu chemistry. The most notable metrical parameters predicted by DFT of **2** and listed in Table 2 are as follows: (1) an O−O bond length of 1.463 Å, (2) an intermetallic Fe···Cu distance of 3.727 Å, (3) slightly inequivalent Cu−O bond lengths of 2.094 and 2.001 Å (compared to the η^1 structure of **1**, where a Cu−O bond length of 1.945 Å is calculated), (4) slightly inequivalent Fe−O bond lengths of 2.060 and 1.902 Å, (5) a slight butterfly of the peroxo core characterized by an Fe−O−O−Cu dihedral angle of 166.1°, and (6) displacement of the Fe out of the pseudoplane of the porphyrn by 0.53 Å. In general, the structural parameters predicted by theory are in good agreement with those measured by Fe

(44) Wasser, I. M.; Huang, H. W.; Moenne-Loccoz, P.; Karlin, K. D. *J. Am. Chem. Soc.* **2005**, *127*, 3310–3320.

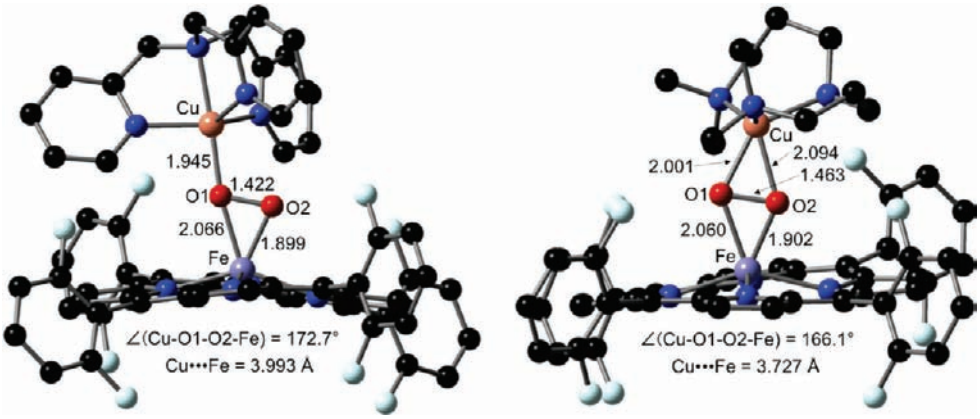

Figure 5. Unrestricted DFT (BS, $S_T = 2$)-optimized molecular structures of **1** (right) and **2** (left). H atoms are omitted for clarity.

Table 2. Selected DFT-Optimized Bond Distances (Å) and Angles (deg) of Models **1** and **2**

	DFT-optimized coordinates	
	1	**2**
Cu−O	1.945, 2.764	2.094, 2.001
O−O	1.433	1.463
Fe−O	2.066, 1.889	2.060, 1.902
Fe···Cu	3.994	3.727
Cu−O−O	109.4	72.5, 65.7
Fe−O−O	75.7, 62.4	74.2, 62.7
Fe−O−O−Cu	172.7	166.1

and Cu K-edge EXAFS. In particular, DFT predicts an intermetallic distance (3.727 Å) in good agreement with the Fe···Cu vector observed from Cu and Fe EXAFS (3.63 Å). Furthermore, the predicted O−O bond length (1.463 Å) is well within the classical peroxo manifold. Analytical frequency calculations were performed on **1** and **2**, yielding ν_{O-O} energies of 889 and 821 cm^{-1}, respectively, which parallel the observed ordering and difference of 810 and 756 cm^{-1} derived experimentally in **1** compared to **2**. Thus, the optimized core is well described by the calculations. Alternative coordination modes were assessed to ensure that a global minimum had been obtained. Specifically, a μ-η^2:η^1 core geometry was found to be a local minimum on the HS potential energy surface. However, this coordination mode lies higher in energy than μ-η^2:η^2 (by ~65 kcal/mol) and deviates from the experimentally observed Fe···Cu distance by 0.5 Å (the predicted distance for this coordination mode is ~4.2 Å).

Electronic Structure. In agreement with the experimentally determined spin of the complexes, both molecules are well described by broken-symmetry wave functions, yielding $S_T = 2$ ground-state electronic structures, in which Fe^{III} and Cu^{II} are antiferromagnetically coupled. In both molecules, one α-hole is localized on the Cu, whereas five β-holes are localized on the Fe (Figures 7 and 8).[45] The magnitudes of the coupling in **1** and **2** between the $S_T = 2$ and 3 states, $|-6J|$, calculated using eq 1, are 4552

$$^4E = \frac{6^{BS}E - {}^6E(\langle S^2\rangle_{BS} - 6)}{12 - \langle S^2\rangle_{BS}} \quad (1)$$

and 4627 cm^{-1}, respectively (using the Hamiltonian $-2JS_1 \cdot S_2$), and is in general agreement with the experimentally observed strong antiferromagnetic coupling. However, the nature of the ligands on Cu, specifically the denticity, engenders distinct character to the singly occupied, and thus net bonding, orbital on the Cu. In the case of **1**, given the propensity of TMPA for five-coordinate trigonal-bipyramidal molecular geometry with O_2^{2-} bound in a end-on fashion, the singly occupied orbital is of $3d_{z^2}$ character. In contrast, with the less conformationally demanding AN ligand, which allows for square-pyramidal geometry and bidentate O_2^{2-}, the singly occupied Cu d orbital of **2** is of $3d_{x^2-y^2}$ character. As depicted graphically in Figure 6, the superexchange pathways in **1** and **2** are via the σ-bonding framework. Specifically, the coupling involves the $3d_{xz}$ orbital of the Fe (z perpendicular to the heme plane and x parallel to the O−O vector) with the singly occupied orbital of the Cu, $3d_{z^2}$ of $3d_{x^2-y^2}$, respectively in **1** and **2**.

In both molecules, the Fe−O_2^{2-} bonding is characterized by two interactions (Figures S5 and S6 in the Supporting Information). The in-plane σ interaction is between the Fe $3d_{xz}$ and O_2^{2-} π^*_σ orbitals, and the out-of-plane δ interaction is between the Fe d_{xy} and O_2^{2-} π^*_ν orbitals. The orbital bases for the interactions are similar in **1** and **2** but do reflect the differences in the peroxo−Cu bonding (Tables 3 and 4). In the case of **1**, the spin-down σ-bonding contributions are 12.0% and 39.4% for O_2^{2-} and Fe (Figure 7 and Table 3; orbital β310) and the δ-bonding contributions are 15.9% and 76.7% for O_2^{2-} and Fe (Figure 7 and Table 3; orbital β303). In **2**, the spin-down σ-bonding contributions are 18.5% and 61.9% for O_2^{2-} and Fe (Figure 8 and Table 4; orbital β284) and the δ-bonding contributions are 13.4 and 80.5% for O_2^{2-} and Fe (Figure 8 and Table 4; orbital β279). Given that the iron porphyrin fragments in **1** and **2** are identical, any differences in bonding must be a result of modulation of the Cu fragment−peroxo bonding. As can be observed from the unoccupied spin-up Cu−O_2^{2-} antibonding molecular orbital of **1**, Cu $3d_{z^2}$ (38.7%) interacts strongly with the in-plane O_2 π^*_σ (31.9%), which does contain some contribution from the Fe (10.9%) and ligands (Figure 7 and Table 3; orbital α307). The unfilled spin-up Cu−O_2^{2-} antibonding orbital of **2** indicates σ overlap of the $3d_{x^2-y^2}$ (41.4%) with the in-plane O_2 π^*_σ (29.6%), with some Fe (9.7%) and ligand contributions (Figure 8

(45) We use the "holes" here to reflect uncompensated occupied valence orbitals; the Cu^{II} has negative spin density and the Fe^{III} has positive spin density.

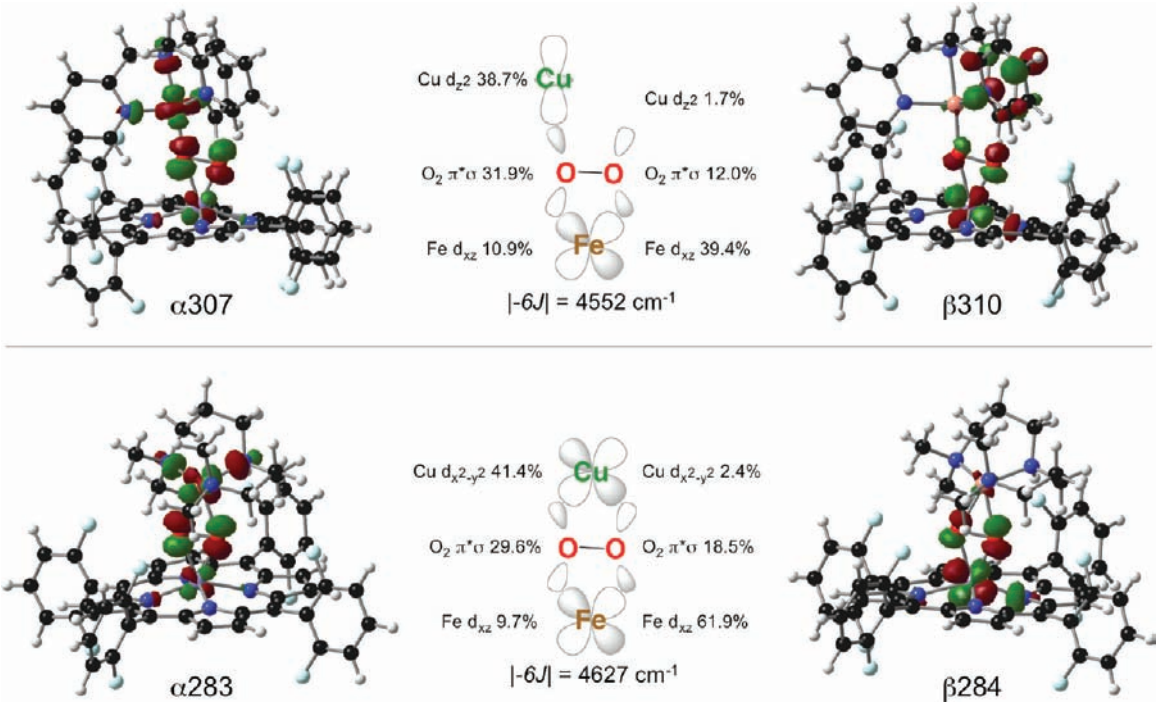

Figure 6. Isosurface plots (0.05 isovalue) and schematic diagrams of the dominant superexchange pathways of **2** (top) and **1** (bottom).

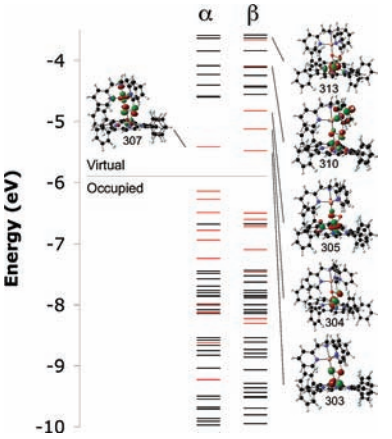

Figure 7. Isosurface plots (isovalue 0.05 au) of unfilled Cu and Fe d orbitals of **1** from a spin-unrestricted BP86 calculation in the BS (S_T = 2) state.

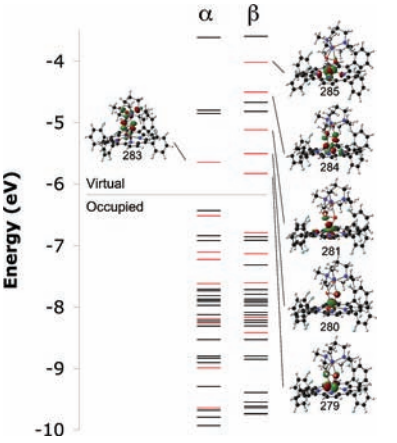

Figure 8. Isosurface plots (isovalue 0.05 au) of unfilled Cu and Fe d orbitals of **2** from a spin-unrestricted BP86 calculation in the BS (S_T = 2) state.

and Table 4; orbital α283). In both molecules, the out-of-plane O_2 π^*_ν is largely nonbonding with the otherwise filled Cu d manifold.

Comparison to the bonding observed in μ-η^2:η^2 and μ-η^1:η^1 Cu_2O_2 homodimers is instructive.[46] In the side-on peroxo complex, [{Cu(Tp)}$_2$(O_2)], which displays a relatively low ν_{O-O} of ~760 cm^{-1}, the unoccupied Cu d−O_2 π^*_σ orbital was calculated to be composed of 68% Cu and 22% O_2. In contrast, in the end-on complex [{Cu(TMPA)}$_2$(O_2)]$^{2+}$, which displays a ν_{O-O} of 830 cm^{-1}, the unoccupied Cu d−O_2 π^*_σ orbital consists of 43% Cu and 9% O_2. Thus, the low intraperoxide stretch observed in the side-on case was not a result of differences in the σ-bonding framework (i.e., in the side-on complex [{Cu(Tp)}$_2$-(O_2)], the peroxo is a better π^*_σ donor, which removes e$^-$ density from an antibonding orbital and, thus, ν_{O-O} should be greater) but rather backbonding into the O_2^{2-} σ^* (O_2^{2-} σ^* mixing into occupied, predominantly Cu d orbitals).[47] On this basis, the ~2.3% calculated difference in the Cu−O_2 covalency in the σ frameworks of **1** and **2** does not sufficiently explain the ~50 cm^{-1} downward shift in the intraperoxide stretching energy observed experimentally between **1** and **2** (**2** having more π^*_σ character) and reproduced by DFT calculations. The more covalent (as defined by the mixing of the filled peroxo π^*_σ orbital into the unfilled Cu d orbital) σ interaction, in fact, would argue for a *higher*

(46) Chen, P.; Fujisawa, K.; Helton, M. E.; Karlin, K. D.; Solomon, E. I. *J. Am. Chem. Soc.* **2003**, *125*, 6394–6408.

(47) Henson, M. J.; Mahadevan, V.; Stack, T. D. P.; Solomon, E. I. *Inorg. Chem.* **2001**, *40*, 5068–5069.

Table 3. Mulliken Population Analysis of Molecular Orbitals from a Spin-Unrestricted BP86 Calculation of **1** in the BS (S_T = 2) State

orbital	level	occ	E (eV)	Cu	O_2	Fe	rest
α307	Cu−O_2 π^*_σ	0	−5.417	38.7	31.9	10.9	18.5
β313	Fe $d_{x^2-y^2}$	0	−3.661	0.1	2.46	67.5	30.0
β310	Fe d_{xz}	0	−4.108	1.7	12.0	39.4	47.0
β305	Fe d_{z^2}	0	−4.825	2.3	6.2	70.4	21.1
β304	Fe d_{yz}	0	−5.126	0.0	9.2	66.2	24.7
β303	Fe d_{xy}−O_2 π^*_ν	0	−5.482	1.2	15.9	76.7	6.2
		spin density		−0.36	0.20, 0.02	3.76	

Table 4. Mulliken Population Analysis of Molecular Orbitals from a Spin-Unrestricted BP86 Calculation of **2** in the BS (S = 2) State

orbital	level	occ	E (eV)	Cu	O_2	Fe	rest
α283	Cu−$O_2\pi^*_\sigma$	0	−5.653	41.4	29.6	9.7	19.3
β285	Fe $d_{x^2-y^2}$	0	−4.021	0.3	2.5	68.3	28.9
b284	Fe d_{xz}	0	−4.508	2.4	18.5	61.9	17.2
β281	Fe d_{z^2}	0	−5.121	1.2	5.9	75.6	17.3
β280	Fe d_{yz}	0	−5.511	0.6	5.6	72.6	21.2
β279	Fe d_{xy}−O_2 π^*_ν	0	−5.834	0.5	13.4	80.5	5.7
		spin density		−0.56	0.10, −0.19	0.85	

ν_{O-O} in **2**, inconsistent with experiment. Differences in mechanical coupling as a rationale to account for the lower intraperoxide stretch were also considered but determined to be negligible by a systematic increase of the mass of the Cu-bound ligand atoms. Surveying the occupied valence orbitals of **1** and **2** for O_2^{2-} σ^* character indicates approximately 4 times greater σ^* character in the occupied valence orbitals of **2** compared to those of **1**. σ^* in **2** acts as a π acceptor, which weakens the O−O bond, leading to a low ν_{O-O} stretching energy. Because of the fact that the σ^* orbital is strongly antibonding, a few percent increase of the mixing of the σ^* character into an occupied metal-based orbital is enough to greatly impact the observed ν_{O-O}. Thus, as in the Cu_2O_2 dimers, the low observed ν_{O-O} in **2** is a result of σ^* backbonding in the μ-η^2:η^2 core structure.

Thermal Decomposition of 1 and 2. The thermal decomposition of HS heme−peroxo−Cu complexes **1** and **2** yields the corresponding μ-oxo compound $[(F_8)Fe^{III}(O^{2-})Cu^{II}(TMPA)]^+$ (**1a**) and $[(F_8)Fe^{III}(O^{2-})Cu^{II}(AN)]^+$ (**2a**) with distinct UV−vis bathochromic shifts in their Soret and Q bands (**1**, λ_{max} = 412 and 526 nm;[48] **1a**, λ_{max} = 433 and 553 nm;[49,50] **2**, λ_{max} = 418, 538, and 561 nm; **2a**, λ_{max} = 440 and 557 nm). The μ-oxo complexes also have distinct ^{1}H NMR features at −80 °C with a pyrrole resonance signal at ∼105 ppm. Separate measurements[29] indicate that ∼0.5 equiv of O_2 is released during the μ-peroxo to μ-oxo conversion, indicating that this process involves a disproportionation reaction, $2[Fe^{III}(O_2^{2-})Cu^{II}]^+ \rightarrow 2[Fe^{III}(O^{2-})Cu^{II}]^+ + O_2$. Insights into the mechanism(s) for such reactions have not been sought or obtained, but similar kinds of processes are known and studied for related nonheme diiron species.[51,52]

X-ray Structure of μ-Oxo Complex $[(F_8)Fe^{III}$-(O^{2-})-$Cu^{II}(AN)]^+$ (2a). The comparison between a new X-ray structure of **2a**, presented here (also see the Supporting Information), and the previously described X-ray structure of **1a**[49] (Figure 9) reveals that in both cases the metal−oxygen bond distances are all similar and characteristically short.[53,54] The Fe−O bond lengths in **1a** [1.740 Å] and **2a** [1.747 Å] are similar to those of μ-oxodiiron(III) porphyrinates,[55] and the short Cu−O bond distances [1.856 Å in **1a** and 1.815 Å in **2a**] are not far off from values observed for bis(μ-oxo)dicopper(III) complexes (Cu−O = 1.8 Å).[33,56] To further compare, a HS (heme)iron(III) hydroxide Fe−O bond length is 1.86 Å,[57] while, for example, copper(II) hydroxide Cu−O(H) bond lengths in complexes with the Cu^{II}−O-(H)−Fe^{III} (1.89−1.95 Å)[50,58] or $Cu^{II}_2(OH^-)_2$/$Cu^{II}(OH^-)$ core (1.9−2.0 Å) are greater.[59−67]

Most interestingly, there is a large difference in the ∠Fe−O−Cu bond angle between the two structures. Complex **1a**, like most other (porphyrinate)-Fe^{III}−O−Cu^{II} complexes with tetradentate Cu ligands,[4,6] have near-linear core structures, but the Fe−O−Cu bridge in **2a** is severely bent to an angle of 149.5°, as is observed in the other complex $[(F_8)Fe^{III}OCu^{II}(L^{Me_2}N)]^+$ (**6**) with a tridentate Cu ligand.[38] We note that a somewhat related μ-hydroxo complex, [(OEP)Fe(OH)Cu(Me5dien)-($OClO_3$)](ClO_4) {OEP = octaethylporphyrinate($^{2-}$); Me5dien = tris[2-[*N*,*N*-dimethylamino)ethyl]amine]}, possesses a bent $Fe^{III}(OH^-)Cu^{II}$ core (∠Fe−OH−Cu = 157.0°),[58] as would be expected for a protonated oxo group changing its hybridzation from sp (μ-oxo) to sp^2 (μ-hydroxo). For the μ-oxo complexes **1a** and **2a**, the differences in observed structures once again illustrate how the nature of the Cu

(48) Chufán, E. E.; Karlin, K. D. *J. Am. Chem. Soc.* **2003**, *125*, 16160–16161.
(49) Karlin, K. D.; Nanthakumar, A.; Fox, S.; Murthy, N. N.; Ravi, N.; Huynh, B. H.; Orosz, R. D.; Day, E. P. *J. Am. Chem. Soc.* **1994**, *116*, 4753–4763.
(50) Fox, S.; Nanthakumar, A.; Wikström, M.; Karlin, K. D.; Blackburn, N. J. *J. Am. Chem. Soc.* **1996**, *118*, 24–34.
(51) Du Bois, J.; Mizoguchi, T. J.; Lippard, S. J. *Coord. Chem. Rev.* **2000**, *200−202*, 443–485.
(52) Feig, a. L.; Becker, M.; Schindler, S.; van Eldik, F.; Lippard, S. J. *Inorg. Chem.* **2003**, *42*, 3704–3704.
(53) Scheidt, W. R.; Reed, C. A. *Chem. Rev.* **1981**, *81*, 543–555.
(54) Obias, H. V.; van Strijdonck, G. P. F.; Lee, D.-H.; Ralle, M.; Blackburn, N. J.; Karlin, K. D. *J. Am. Chem. Soc.* **1998**, *120*, 9696–9697.
(55) Kurtz, D. M., Jr. *Chem. Rev.* **1990**, *90*, 585–606.
(56) Que, L., Jr.; Tolman, W. B. *Angew. Chem., Int. Ed.* **2002**, *41*, 1114–1137.
(57) Yeh, C.-Y.; Chang, C. J.; Nocera, D. G. *J. Am. Chem. Soc.* **2001**, *123*, 1513–1514.
(58) Scott, M. J.; Zhang, H. H.; Lee, S. C.; Hedman, B.; Hodgson, K. O.; Holm, R. H. *J. Am. Chem. Soc.* **1995**, *117*, 568–569.
(59) Lee, S. C.; Holm, R. H. *Inorg. Chem.* **1993**, *32*, 4745–4753.
(60) Koval, I. A.; van der Schilden, K.; Schuitema, A. M.; Gamez, P.; Belle, C.; Pierre, J. L.; Luken, M.; Krebs, B.; Roubeau, O.; Reedijk, J. *Inorg. Chem.* **2005**, *44*, 4372–4382.
(61) Mahapatra, S.; Halfen, J. A.; Wilkinson, E. C.; Pan, G.; Wang, X.; Young, J., V. G.; Cramer, C. J.; Que, J., L.; Tolman, W. B. *J. Am. Chem. Soc.* **1996**, *118*, 11555–11574.
(62) Berreau, L. M.; Mahapatra, S.; Halfen, J. A.; Young, V. G.; Tolman, W. B. *Inorg. Chem.* **1996**, *35*, 6339-&.
(63) Obias, H. V.; Lin, Y.; Murthy, N. N.; Pidcock, E.; Solomon, E. I.; Ralle, M.; Blackburn, N. J.; Neuhold, Y.-M.; Zuberbühler, A. D.; Karlin, K. D. *J. Am. Chem. Soc.* **1998**, *120*, 12960–12961.
(64) Shearer, J.; Zhang, C. X.; Zakharov, L. N.; Rheingold, A. L.; Karlin, K. D. *J. Am. Chem. Soc.* **2005**, *127*, 5469–5483.
(65) Izzet, G.; Akdas, H.; Hucher, N.; Giorgi, M.; Prange, T.; Reinaud, O. *Inorg. Chem.* **2006**, *45*, 1069–1077.
(66) Hong, S.; Hill, L. M. R.; Gupta, A. K.; Naab, B. D.; Gilroy, J. B.; Hicks, R. G.; Cramer, C. J.; Tolman, W. B. *Inorg. Chem.* **2009**, *48*, 4514–4523.
(67) Contaldi, S.; Nicola, C. D.; Garau, F.; Karabach, Y. Y.; Martins, L. M. D. R. S.; Monari, M.; Pandolfo, L.; Pettinari, C.; Pombeiro, A. J. L. *Dalton Trans.* **2009**, 4928–4941.

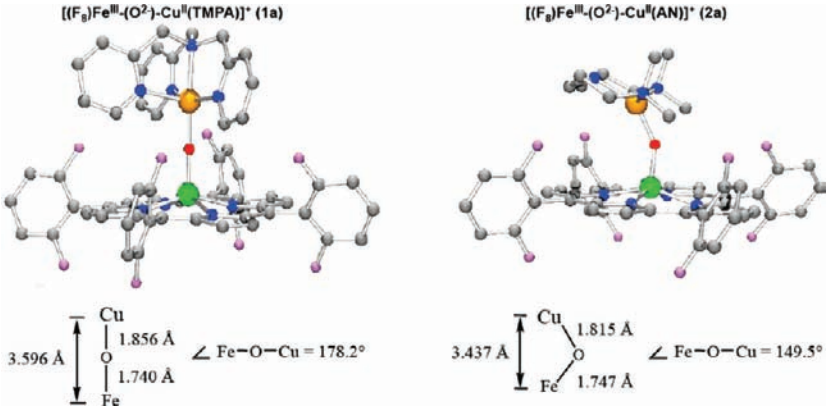

Figure 9. Core structure depiction of μ-oxo complexes **1a** and **2a**. An ORTEP diagram of the cationic portion of **2a** along with other X-ray crystallographic data is given in the Supporting Information.

chelate (tri- vs tetradentate) influences the structure of the heme−Cu−O_2 adducts. Such structural (Chart 2) and reactivity effects are already well-known in Cu−O_2 chemistry.[31,32,68]

Reactivity of HS Heme−Peroxo−Cu Complexes 1 and 2. We have previously[37] described the reactivity of **1** and **2**, along with peroxo complexes **3** and **4** (Chart 1), toward different reagents, HCl, $Co(Cp)_2$, CO, PPh_3, and *tert*-butyl-substituted phenols. Because an important goal of the current report is to contrast the reactivity when the spin state of the heme-Fe is changed (vide infra), we summarize here major aspects of the reactivity observed for the HS complexes **1** and **2** (Scheme 3).

Hydrochloric acid (HCl) was added to **1** and **2**, in order to study the possibility of forming and studying protonated O_2 species (e.g., hydroperoxo complexes).[9,10,12] Protonation and formation of such species are likely important in triggering HCO enzymatic O−O reductive cleavage events. When peroxo complexes **1** and **2** were exposed to 1 or 2 equiv of HCl, neither low-temperature UV−vis nor ^{1}H NMR spectroscopic investigations showed any evidence for a hydroperoxo intermediate; i.e., the formation of a new absorption feature was not found in the reaction. Further, electron paramagnetic resonance (EPR) spectroscopic and electrospray ionization mass spectrometry (ESI-MS) analyses of the reaction products revealed the formation of $F_8Fe^{III}Cl$ and $Cu^{II}Cl$. H_2O_2 was released, providing complementary evidence that O_2 adducts **1** and **2** have a peroxidic nature.[37]

Peroxo complexes **1** and **2** possess O_2 in its two-electron-reduced state. Thus, to complete the reductive cleavage of O_2 to the level of water, two more electrons are needed. The strong outer-sphere reductant cobaltocene ($CoCp_2$) was, thus, used to provide these reducing equivalents.[29,37,48] The reaction of 2 equiv of $CoCp_2$ does effect O−O cleavage and the formation of the corresponding previously structurally characterized μ-oxo-bridged compounds **1a** and **2a**.[37] This result differs from an earlier work of Collman and co-workers, where they showed that the addition of $CoCp_2$ to heme−O_2−Cu complexes containing an appended imidazole axial base for iron led to fully reduced Fe^{II}/Cu^{I} and the reduction of O_2 to H_2O_2.[69−72]

1 and **2** were also exposed to carbon monoxide and PPh_3,[37] reagents known to either displace the peroxide or to be subject to oxidation, giving CO_2 [in the case of CO (in C*c*O)][73] or O=PPh_3 (in the case of triphenylphosphine). Compound **2** reacted with excess CO(g) to form the CO adduct $(THF)(F_8)Fe^{II}CO$ and copper monoxide adduct $[Cu^{I}(AN)(CO)]^+$ while also releasing O_2. Surprisingly, **1** does not react with CO. **2** reacts with PPh_3 to displace the peroxo ligand from Cu, but not from Fe, thus involving a formally partial reduction reaction. The products are the Fe−superoxo species $(solvent)(F_8)Fe^{III}(O_2^{\bullet-})$ and the reduced copper(I) phosphine adduct $[Cu^{I}(AN)(PPh_3)]^+$. Interrogation of the product solutions using ^{31}P NMR spectroscopy showed only the presence of PPh_3 (and no O=PPh_3). Unexpectedly, complex **1** displays no reaction toward PPh_3 under these conditions. In summary, there are clear differences in $Fe^{III}(O_2^{2-})Cu^{II}$ reactions with CO or PPh_3 that reflect variations in the detailed nature of the peroxo structure and reactivity induced by the nature of the Cu ligand (tri- vs tetradentate).

The examination of the addition of phenols to heme−Cu−O_2 adducts was inspired by the reactivity observed for the "mixed-valent" C*c*O enzyme form, wherein an active-site tyrosine, found crystallographically to be covalently tethered to a Cu-bound histidine, is thought to act as a net H-atom donor (see the Introduction and further discussion below).[4] When either 2,4-di-*tert*-butylphenol or 2,4,6-tri-*tert*-butylphenol, i.e., good H-atom ($H^+ + e^-$) donors, was added to low-temperature solutions of **1** or **2**, no reaction occurred (Scheme 3). This is an important finding, especially when contrasted with the chemistry of a LS analogue (vide infra).

Collman and co-workers[74] recently reported that a phenol as H-atom source can be added to a

(68) Itoh, S.; Tachi, Y. *Dalton Trans.* **2006**, 4531–4538.
(69) Collman, J. P.; Herrmann, P. C.; Boitrel, B.; Zhang, X.; Eberspacher, T. A.; Fu, L.; Wang, J.; Rousseau, D. L.; Williams, E. R. *J. Am. Chem. Soc.* **1994**, *116*, 9783–9784.
(70) Collman, J. P.; Fu, L.; Herrmann, P. C.; Zhang, X. *Science* **1997**, *275*, 949–951.
(71) Collman, J. P. *Inorg. Chem.* **1997**, *36*, 5145–5155.
(72) Collman, J. P.; Fu, L.; Herrmann, P. C.; Wang, Z.; Rapta, M.; Bröring, M.; Schwenninger, R.; Boitrel, B. *Angew. Chem., Int. Ed.* **1998**, *37*, 3397–3400.
(73) Kim, Y.; Shinzawa-Itoh, K.; Yoshikawa, S.; Kitagawa, T. *J. Am. Chem. Soc.* **2001**, *123*, 757–758.
(74) Collman, J. P.; Decréau, R. A.; Sunderland, C. J. *Chem. Commun.* **2006**, 3894–3896.

Scheme 3

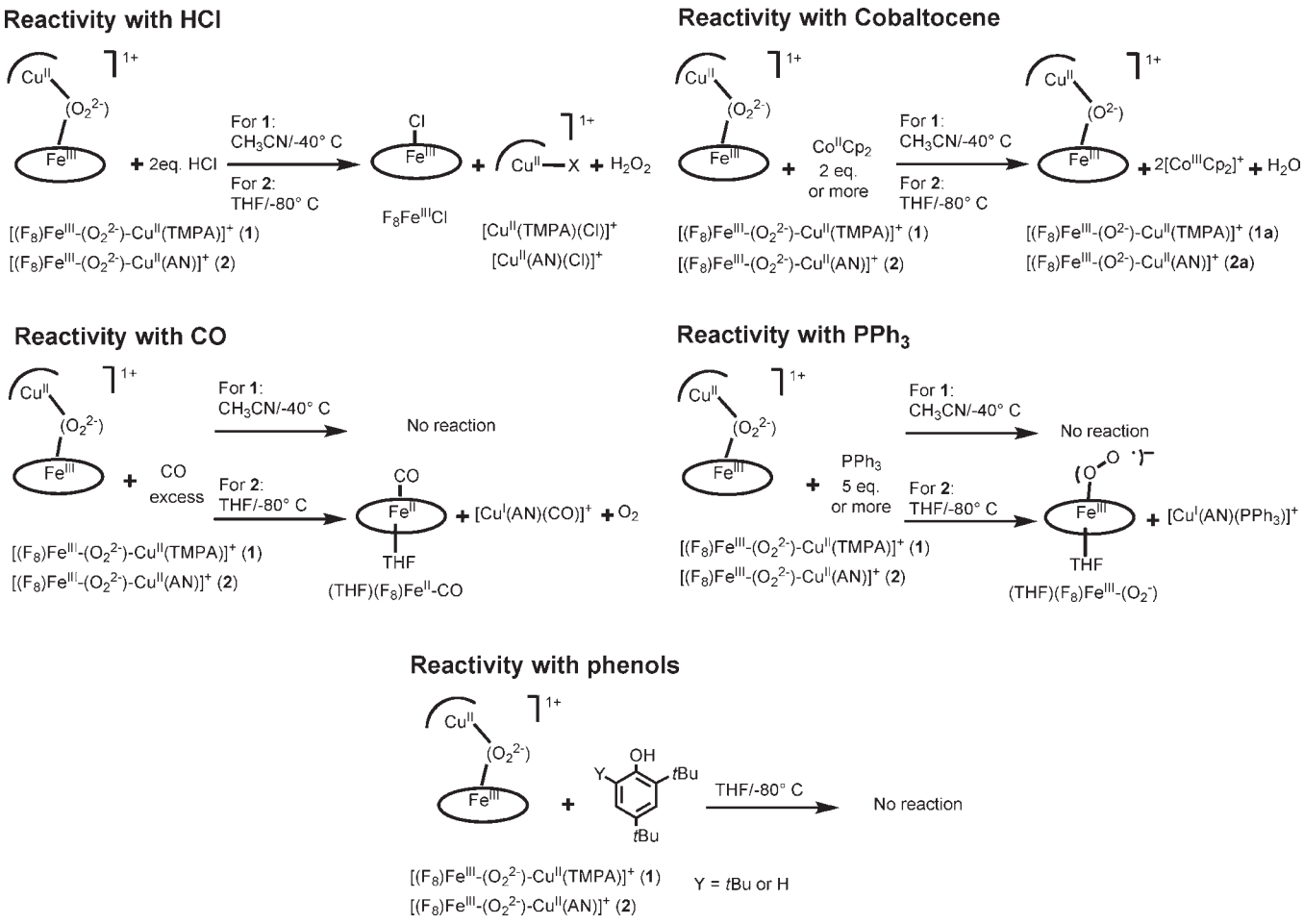

heme−superoxo−Cu complex (i.e., a LS $Fe^{III}(O_2^{\bullet-})\cdots Cu^{I}$ moiety), resulting in reductive O−O cleavage and the formation of a phenoxyl radical (A, Chart 3). This heme−Cu complex possesses an internal (i.e., appended) imidazole axial base for Fe. A closely related complex possessing an internal phenol group (i.e., in which one of the R groups is a phenol; Chart 3A) can electrocatalytically reduce O_2 to water.[22] In that system, electronic structural and spin-state issues have not been addressed beyond the superoxo complex and possible intermediates after O−O cleavage. In systems that we have studied, $(F_8)Fe^{III}(O_2^{-})\cdots Cu^{I}$ species are transient (but detectable) intermediates (Figure 10)[39] in the reduction of O_2 from the $Fe^{II}\cdots Cu^{I}$ to $Fe^{III}(O_2^{2-})Cu^{II}$(ligand) complex stage, the latter being stable at −80 °C and amenable to study, i.e., those complexes in Chart 1.

It is notable that, for nonheme-Fe^{III}−OOR complexes, LS rather than HS species are amenable to reductive O−O cleavage chemistry as a consequence of the weakened peroxide O−O bonds and strengthened Fe−O bonds.[75,76] From all of the information available, as discussed thus far in this report, it was clear one should investigate, compare, and contrast the chemistry of HS $Fe^{III}(O_2^{2-})Cu^{II}$ complexes with LS analogues, if we could generate the latter. This was accomplished, as described below.

Generation of a LS Heme−Peroxo−Cu Complex. The LS heme−O_2−Cu complex, which we formulate as $[DCHIm(F_8)Fe^{III}(O_2^{2-})Cu^{II}(AN)]^+$ (**2b**) was generated by the addition of 1 equiv of 1,5-dicyclohexylimidazole (DCHIm) to a solution of HS **2** in THF at −80 °C (Scheme 4). Collman's research group reported the first example of a well-characterized discrete O_2 adduct in a heme−Cu assembly using a sophisticated superstructured "capped" porphyrin with appended triazacyclononane as the ligand for Cu (B, Chart 3).[69,71] When a solution of $[(\alpha_3TACN\alpha Acr)Fe^{II}Cu^{I}]^+$ is mixed with a large excess (500 equiv) of DCHIm and subsequently exposed to O_2, the rapid and irreversible formation of a LS adduct $[(DCHIm)(\alpha_3TACN\alpha Acr)Fe^{III}(O_2^{2-})Cu^{II}]^+$ occurs.

With our system, the UV−vis monitoring shows that only 1 equiv of DCHIm is required for the complete transformation of HS species **2** (418, 538, and 561 nm) to LS species **2b** (421 and 537 nm) (Figure 11). An ^2H NMR study of **2b** formation was performed using a pyrrole-deuterated version of F_8 (Figure 12). After generation of the HS peroxo **2** (pyrrole resonance at ∼95 ppm), the addition of 1 equiv of DCHIm is accompanied by a shift of the pyrrole signal to the diamagnetic region ($\delta_{pyrrole}$ ∼ 8.3 ppm). This behavior suggests that in **2b** the presence of antiferromagnetic coupling between the LS ($S = {}^1/_2$) six-coordinate Fe^{III} and the d^9 Cu^{II} (also $S = {}^1/_2$) centers

(75) Lehnert, N.; Ho, R. Y. N.; Que, L., Jr.; Solomon, E. I. *J. Am. Chem. Soc.* **2001**, *123*, 12802–12816.
(76) Lehnert, N.; Ho, R. Y. N.; Que, L., Jr.; Solomon, E. I. *J. Am. Chem. Soc.* **2001**, *123*, 8271–8290.

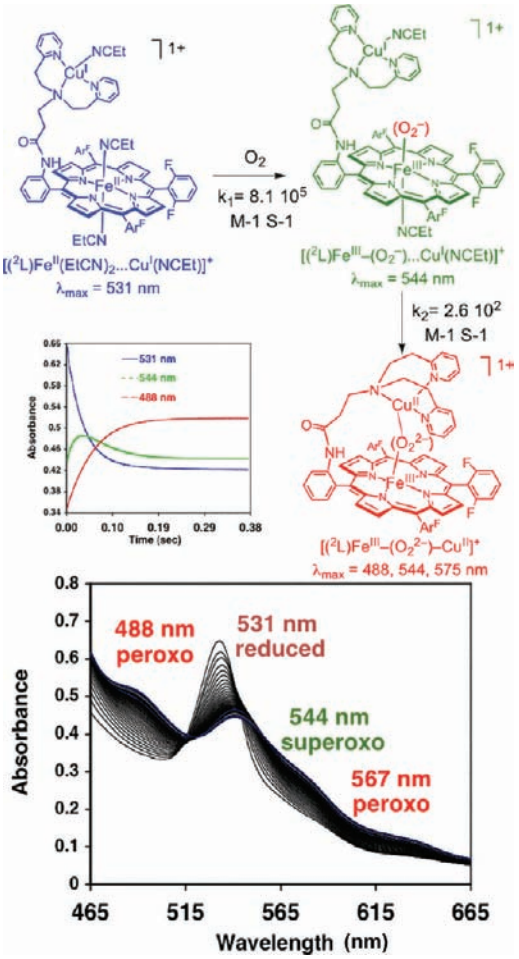

Figure 10. UV−vis detection of the transient $[(^2L)Fe^{III}(O_2^-)\cdots Cu^I(NCEt)]^+$ preceding the formation of $[(^2L)Fe^{III}(O_2^{2-})Cu^{II}(NCEt)]^+$ by oxygenation of $[(^2L)Fe^{II}\cdots Cu^I(NCEt)]^+$ at −90 °C in 6% EtCN/CH_2Cl_2.

Chart 3

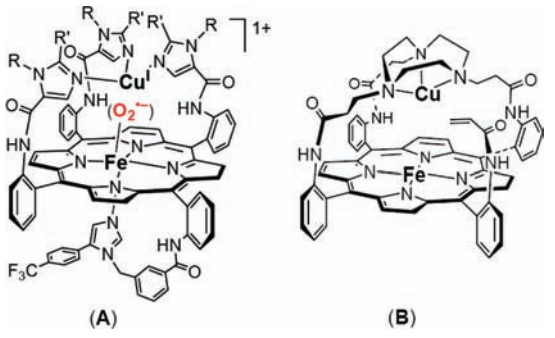

occurs through the peroxo bridge. The latter's peroxidic nature is not yet unequivocally determined.[77] However, evidence that **2b** possesses a peroxidic intact O−O bond is suggested by its reactivity with HCl to release hydrogen peroxide in good yield (see the Experimental Section). Alternative formulations of the new species **2b** as either (1) a mixture of $(F_8)Fe^{III}(O_2^{2-})Fe^{III}(F_8)$ ($\delta_{pyrrole}$ = 15−19 ppm},[26] and $[(AN)Cu^{II}(O_2^{2-})Cu^{II}(AN)]^+$ (formed

(77) Experiments to assign the structure of **2b** are in progress.
(78) Balch, A. L. *Inorg. Chim. Acta* **1992**, *198*−*200*, 297–307.

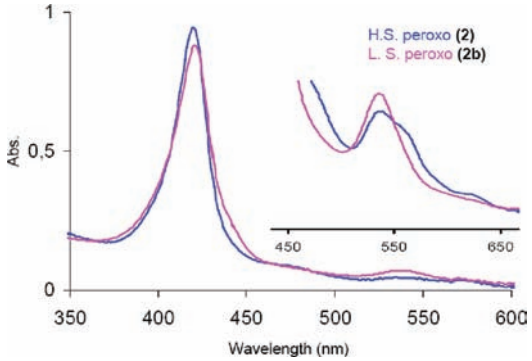

Figure 11. UV−vis spectra monitoring the generation of the LS peroxo complex **2b** (λ_{max} = 421 and 537 nm) from the HS peroxo complex **2** (λ_{max} = 418, 538, and 561 nm) in THF at −80 °C.

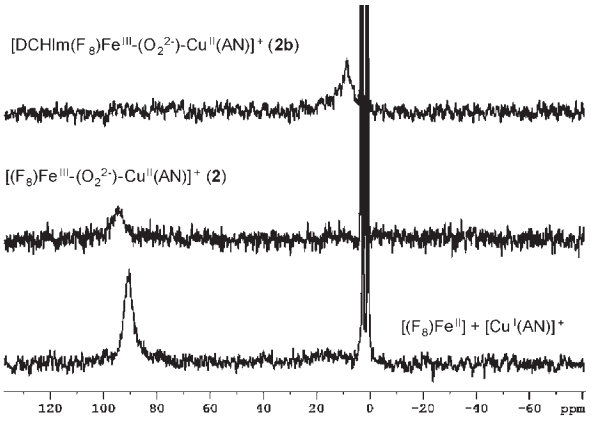

Figure 12. ^2H NMR spectra of the generation of **2** and **2b** successively from oxygenation of a 1:1 mixture of $[Cu^I(AN)]^+$ and the pyrrole-deuterated version of $[(F_8)Fe^{II}]$ (acetone-d^6 at − 80 °C).

Scheme 4

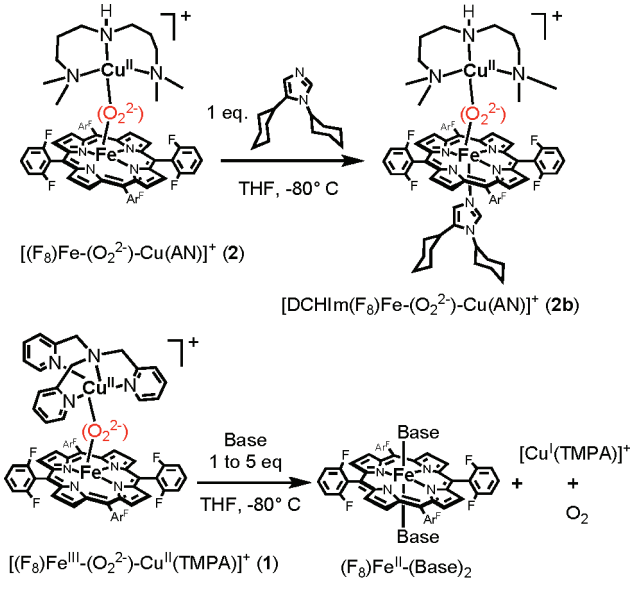

by disproportionation of **2b**) or (2) a O−O cleaved[78] product to give ferryl complex $[(DCHIm)(F_8)Fe^{IV}{=}O]$ (**2c**; $\delta_{pyrrole}$ 4−5 ppm) can be ruled out based on its

$\delta_{pyrrole} \sim 8.3$ ppm assignment and UV−vis spectroscopic peak positions.[41] The formation of an analogous complex to **2b** was also observed using 4-(dimethylamino)pyridine (DMAP) instead of DCHIm as the exogenous axial ligand.

By contrast, the addition of an axial base such as DCHIm or DMAP to a solution of **1** effects the release of O_2 and the formation of a mixture of $[Cu^{I}(TMPA)]^{+}$ and six-coordinate LS compound $(F_8)Fe^{II}(Base)_2$ (Scheme 4). The reaction was followed by UV−vis spectroscopy, as shown in the Supporting Information (Figure S2): the peroxo compound **1** exhibits a Q band at 558 nm with a shoulder at 535 nm (CH_3CN, − 40 °C), and upon the addition of 1 to 5 equiv of DMAP, a new spectrum with $\lambda_{max} = 527$ nm is formed and assigned to $(F_8)Fe^{II}(DMAP)_2$. To support this assignment, a control experiment was conducted in which the addition of DMAP to a solution of the mixture of $(F_8)Fe^{II}/[Cu^{I}(TMPA)]^{+}$ yielded the same spectrum because of the formation of $(F_8)Fe^{II}(DMAP)_2$. The evolution of 0.9 equiv of O_2 was determined by exposing evolved gases to an alkaline pyrogallol test solution;[79] within experimental error, this finding is consistent with the quantitative oxidation of the peroxide moiety to molecular oxygen.

Reactivity of the LS Peroxo Complex 2b toward Phenols. To study the reactivity of the LS peroxo complex **2b** toward phenols, 2,4-di-*tert*-butylphenol was employed first as the substrate. The rationale for the selection of this phenol was if H-atom abstraction ($H^{+} + e^{-}$) occurred, the phenol would couple to form 3,3′,5,5′-tetra-*tert*-butyl-2,2′-dihydroxylbiphenyl, which can be detected and quantified as a stable product.[80−84] We have shown above (Scheme 3) that the HS peroxo complex **2** does not react with phenols. The addition of 1 equiv of 2,4-di-*tert*-butylphenol to a solution of the LS peroxo complex **2b** in THF at −80 °C leads to the formation of the coupled phenol product 3,3′,5,5′-tetra-*tert*-butyl-2,2′-dihydroxylbiphenyl (Scheme 5). Gas chromatography−mass spectrometry (GC−MS) analyses of the reaction mixture at room temperature revealed that the yield of the reaction is greater than 65%. Further spectroscopic investigations show that the oxidative coupling of the phenol is accompanied by the reductive cleavage of the peroxo bridge and the formation of copper(II) hydroxide complex ($[Cu^{II}(AN)(OH)]^{+}$) and ferryl heme **2c** (Scheme 5). The evidence for the presence of $[Cu^{II}(AN)(OH)]^{+}$ comes from observation of a characteristic Cu^{II}−OH EPR signal of the frozen reaction mixture ($A_{\|} = 127 \times 10^{-4}\,cm^{-1}$, $A_{\perp} = 35 \times 10^{-4}\,cm^{-1}$, $g_{\|} = 2.24$, and $g_{\perp} = 2.06$) (Figure S3 in the Supporting Information) and from

Scheme 5

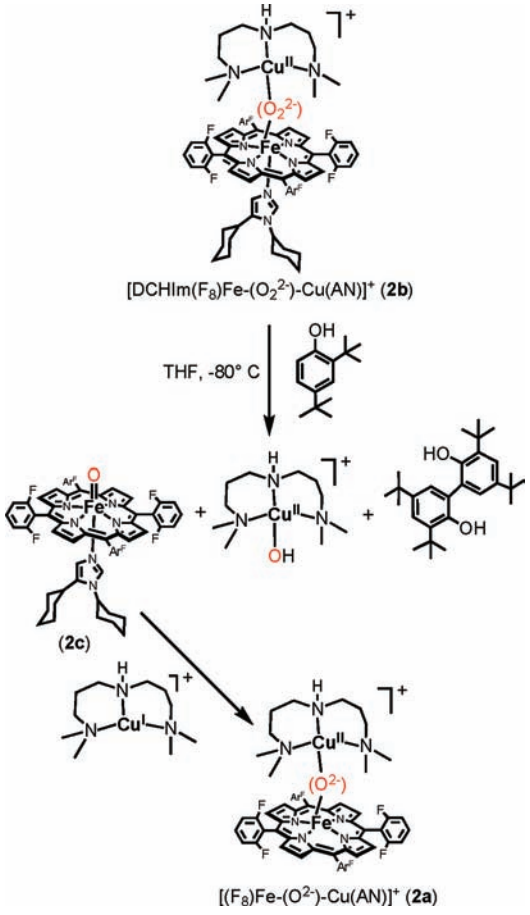

ESI-MS spectrometry at room temperature (calcd m/z 267.1 for $C_{10}H_{26}CuN_3O$; found m/z 267.5). The EPR spectrum of the reaction mixture after warming to room temperature presents the same signal for $Cu^{II}OH$ in addition to a characteristic signal for the well-known stable compound $(F_8)Fe^{III}OH$ ($g = 5.8$), which derives from thermal decay of **2c**.[41] The UV−vis monitoring of the O−O cleavage reaction shows a shift of the **2b** Q band at 535 nm to a new band at 540 nm (Supporting Information, Figure S1). This band was also observed for an authentic $[DCHIm(F_8)Fe^{IV}{=}O]$ generated by the reaction of $[(F_8)Fe^{III}]_2(O_2^{2-})$ with DCHIm in a noncoordinating solvent.[41,85] The ferryl nature of the product solution and the presence of **2c** were also established by its reactivity toward different substrates: (a) the low-temperature addition of 1 equiv of $[Cu^{I}(AN)]^{+}$ leads to the formation of **2a** (90% yield calculated by UV−vis spectroscopy; Scheme 5); the same redox reaction is also observed with the authentic ferryl−(Fe^{IV}=O) complex, as determined in a separate "control" experiment; (b) the addition of triphenylphosphine to the reaction solution led to triphenylphosphine oxide, also a criterion used to demonstrate the presence of a ferryl (Fe^{IV}=O) species.[86]

To confirm the electron and proton transfer from the phenol to **2b** and the formation of the phenoxyl radical

(79) Park, G. Y.; Deepalatha, S.; Puiu, S. C.; Lee, D.-H.; Mondal, B.; Narducci Sarjeant, A. A.; del Rio, D.; Pau, M. Y. M.; Solomon, E. I.; Karlin, K. D. *J. Biol. Inorg. Chem.* **2009**, *14*, 1301–1311.
(80) Paul, P. P.; Tyeklár, Z.; Jacobson, R. R.; Karlin, K. D. *J. Am. Chem. Soc.* **1991**, *113*, 5322–5332.
(81) Lucchese, B.; Humphreys, K. J.; Lee, D.-H.; Incarvito, C. D.; Sommer, R. D.; Rheingold, A. L.; Karlin, K. D. *Inorg. Chem.* **2004**, *43*, 5987–5998.
(82) Halfen, J. A.; Young, V. G., Jr.; Tolman, W. B. *Inorg. Chem.* **1998**, *37*, 2102–2103.
(83) Mahadevan, V.; DuBois, J. L.; Hedman, B.; Hodgson, K. O.; Stack, T. D. P. *J. Am. Chem. Soc.* **1999**, *121*, 5583–5584.
(84) Kushioka, K. *J. Org. Chem.* **1983**, *48*, 4948–4950.
(85) Chin, D. H.; Lamar, G. N.; Balch, A. L. *J. Am. Chem. Soc.* **1980**, *102*, 5945–5947.
(86) Collman, J. P.; Decreau, R. A.; Yan, Y.; Yoon, J.; Solomon, E. I. *J. Am. Chem. Soc.* **2007**, *129*, 5794–5795.

Scheme 6

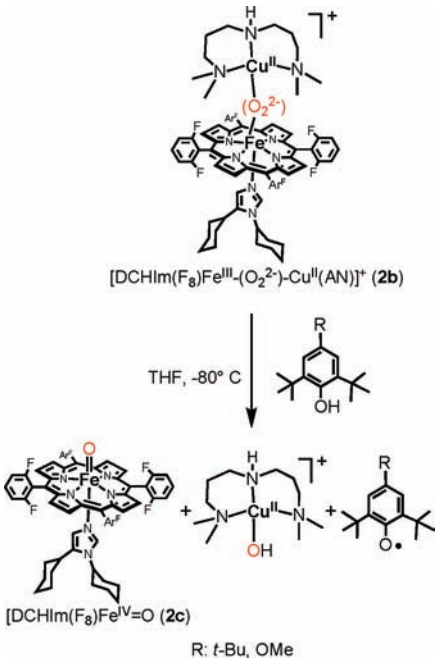

prior to the phenol coupling, we used 2,4,6-tri-*tert*-butylphenol and 2,6-di-*tert*-buyl-4-methoxyphenol (Scheme 6), two phenols known to form relatively stable and detectable phenoxyl radicals.[87−89] The reaction of EPR-silent **2b** with those phenols in THF at −80 °C leads to the formation of the phenoxyl radical, which displays an intense and characteristic EPR signal at 2.006 in the case of 2,4,6-tri-*tert*-butylphenol and at 2.008 in the case of 2,6-di-*tert*-butyl-4-methoxyphenol (Figure 13).

Summary and Perspectives

Our investigation into the nature of heme−peroxo−Cu complexes has revealed that the denticity (tri- vs tetradentate) of the Cu ligand can have a major influence on the molecular structure and the electronic structure and bonding in such species. Using rR and EXAFS spectroscopic analyses coupled to DFT calculations, we have previously established a μ-(O_2^{2-}) side-on to the Fe^{III} ion and an end-on to Cu^{II} (i.e., μ-η^2:η^1-peroxo) center binding in the complex with the tetradentate Cu ligand **1**. However, in new investigations described here, side-on/side-on (μ-η^2:η^2) μ-peroxo coordination for the complex with a tridentate Cu ligand is established for **2**. Insights into the electronic structure and bonding of **2** and comparisons to **1** are described. A structural difference, for tridentate versus tetradentate Cu ligand, was also directly observed by comparison of the X-ray structures of the μ-oxo complexes **1a** and newly reported species **2a**, with these obtained respectively by thermal decomposition of **1** and **2**.

These electronic and structural differences between the two O_2 adducts result in a difference in their reactivities toward substrates such as CO or PPh_3. More interestingly, the difference between the two HS heme−peroxo complexes **1** and **2** is the ability of the latter with tridentate Cu ligand to form a new low-temperature-stable LS complex **2b** in the presence of an axial base, tentatively assigned as a peroxo complex. Under the same conditions, complex **1** (tetradentate Cu ligand) reacts with DCHIm only to break apart the heme−peroxo−Cu assembly, essentially reversing its formation and releasing O_2.

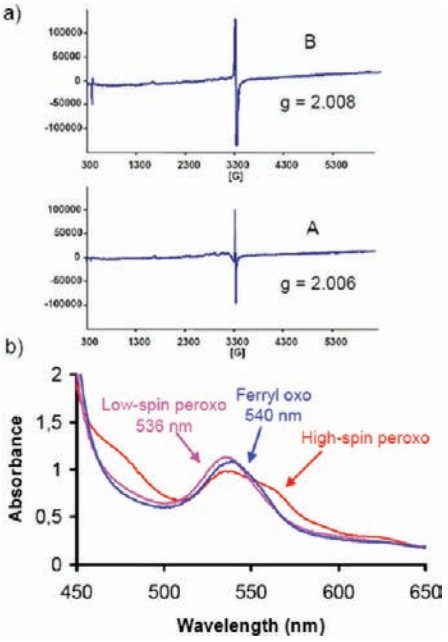

Figure 13. (a) EPR spectra recorded at 77 K of generated phenoxyl radicals by the reaction of **2b** and 2,4,6-tri-*tert*-butylphenol (A) or 2,4-di-*tert*-butyl-4-methoxylphenol (B) at −80 °C in THF. As determined in separate experiments, at equal concentrations of a phenoxyl radical with a Cu^{II} complex, the radical $g \sim 2$ signal peak intensity is vastly greater than the peak intensities for the $g \sim 2.0-2.3$ signals resulting from the Cu^{II} ion due to the differences in the peak width, which is why the latter is essentially not observable. Also, within the resolution of the EPR experiments conducted, the g values are indistinguishable.[90,91] (b) UV−vis monitoring of the reaction of **2b** with 2,4-di-*tert*-butylphenol at −80 °C.

In this study, we have also shown that, in contrast to the behavior of the HS complexes **1** and **2**, the new LS complex **2b** reacts with phenols performing O−O bond cleavage, which is accompanied by the formation of the high-valent ferryl heme species **2c**.[77] This reaction occurs as a net H-atom abstraction ($H^+ + e^-$) from the phenol with generation of a phenoxyl radical.

Given the new reactivity demonstrated by the LS complex, considerable future efforts are needed to determine the geometric and electronic structure of the LS system in comparison to the structure of the HS system determined here. Such comparisons can contribute to a better understanding of the differenential reactivity observed depending on the spin state in addition to different peroxo bridging modes. It is intruiging to consider that if a bridging peroxo species could be identified as a fleeting intermediate in C*c*O, would its spin state also be of central importance? On the basis of chemical precedent and given the proximal histidine present in heme−copper oxidase enzymes, one would surmise that a LS state was at work. Nonetheless, previous studies have suggested heme a_3 proximal histidine dissociation from

(87) Manner, V. W.; Markle, T. F.; Freudenthal, J. H.; Roth, J. P.; Mayer, J. M. *Chem. Commun.* **2008**, 256–258.
(88) Hicks, R. G. *Org. Biomol. Chem.* **2007**, *5*, 1321–1338.
(89) Altwicker, E. R. *Chem. Rev.* **1967**, *67*, 475.
(90) Nakanishi, I.; Fukuhara, K.; Shimada, T.; Ohkubo, K.; Iizuka, Y.; Inami, K.; Mochizuki, M.; Urano, S.; Itoh, S.; Miyata, N.; Fukuzumi, S. *J Chem Soc Perk T 2* **2002**, 1520–1524.
(91) Yamaji, T.; Saiful, I. S. M.; Baba, M.; Yamauchi, S.; Yamauchi, J. *J. Phys. Chem. A* **2007**, *111*, 4612–4619.

iron, a mechanism that is known to occur in the evolutionarily related heme/nonheme diiron NO reductases, suggestive of a HS oxidant.

However, in addition to the spin-state contribution to the O−O bond cleavage in heme−copper oxidases, proton and electron transport must also be considered. The order in which protons and electrons enter catalysis may shed light on the nature of the active oxidant. Our interest is especially piqued by the speculation of a discrete hydroperoxo species (either Cu or Fe bound or both), given the generality of such a potential reaction. As such, we have embarked on studies, some of which are alluded to herein, to test the possibility of such species and their respective reactivity for insight into the mechanism of heme−copper oxidases.

Within the context of (1) the nature of the active oxidant and (2) the role of protons and electrons in driving a particular reaction coordinate, the issue of the active site tyrosine remains intruiging to us from a mechanistic standpoint. While it is generally accepted that a tyrosine radical forms at some point during the reaction, it remains an open question as to when its proton and electron enter the catalytic cycle and by what means. Specifically, (1) does the active site oxidant do direct H-atom abstraction from the tyrosine or does the reaction occur stepwise and (2) do the transfers occur before or after the O−O bond is cleaved? Stepwise mechanisms would indicate the importance of the Tyr−His cross-link to form an adequate superexchange pathway for electron transfer and would significantly enhance the functional role of Cu in mediating the electron transfer. Finally, how would such a cross-link be formed in an active site? Presumably, one would invoke some sort of oxidative coupling involving reduced oxygen species in the proenzyme before the first turnover (the cofactor biogenesis reaction), but would that process require both Cu and Fe? Hopefully, our foray into small-molecule analogues as probes of these potential mechanistic scenarios continues to shed light on these critical questions, given the enormous scope of the processes involved and applicability to problems ranging from disease to energy conversion.

Experimental Section

Materials and Methods. All reagents and solvents were purchased from commercial sources and were of reagent quality unless otherwise noted. Tetrahydrofuran (THF) was distilled from sodium benzophenone under argon, and acetonitrile (CH_3CN) was purified over an activated alumina column. The preparation and handling of air-sensitive compounds were performed under a MBraun Labmaster 130 inert atmosphere (<1 ppm O_2 and <1 ppm H_2O) glovebox filled with nitrogen. The deoxygenation of the solvents was effected either by repeated freeze/pump/thaw cycles or by bubbling with argon for 30−45 min.

Low-temperature UV−vis spectra were recorded on a Hewlett-Packard model 8453A diode-array spectrometer with HP Chemstation software; the instrument was equipped with a variable-temperature Dewar and cuvette. ^1H and ^2H NMR spectra were measured on a Varian XL-400 NMR instrument and a Bruker 400 MHz spectrometer at ambient or low temperatures. All spectra were recorded in 5-mm-o.d. NMR tubes, and chemical shifts δ (ppm) were referenced either to an internal standard (Me_4Si) or to residual solvent peaks. EPR spectra were obtained in frozen solutions with 4-mm-o.d. quartz tubes in a Bruker EMX spectrometer operating at X band using microwave frequencies of around 9.5 GHz, with the sample temperature maintained at 77 K. EPR spectra were referenced to 2,2-diphenyl-1-picrylhydrazyl ($g = 2.0036$). Elemental analyses were performed by Desert Analytics (Tuscon, AZ). The coupled phenol was analyzed by GC−MS on a Shimadzu GC17A/QP5050A instrument equipped with a nonpolar column (DB-5 ms). Helium was used as the carrier gas at a flow rate of 27 cm s^{-1}. Injections were made in split mode using an initial column temperature of 100 °C. The temperature was raised by 20 °C/min to 300 °C with initial and final hold times of 3 and 2 min, respectively.

XAS Data Acquisition. The Cu and Fe K-edge XAS spectra of $[(F_8)Fe^{III}O_2Cu^{II}(AN)](ClO_4)$ in solution form were measured at the Stanford Synchrotron Radiation Lightsource (SSRL) on the focused 16-pole, 2.0-T wiggler beamline 9-3 under storage ring parameters of 3 GeV and 80−100 mA. A Rh-coated premonochromator flat bent mirror was used for harmonic rejection and vertical collimation, while a bent cylindrical Rh-coated postmonochromator mirror was used for focusing. A Si(220) double-crystal monochromator was used for energy selection. A total of ~150 μL each of the solution samples was loaded into 2 mm Delrin XAS cells with a 38 μm Kapton window. The samples were immediately frozen and stored under liquid nitrogen. The samples were maintained at a constant temperature of ~10 K during data collection using an Oxford Instruments CF 1208 continuous-flow liquid-helium cryostat. A Canberra solid-state Ge 30-element array detector was used to collect Kα fluorescence data. Data reported here are up to $k = 12.8$ Å^{-1} for Cu in order to avoid interference from the Zn K-edge and up to $k = 16$ Å^{-1} for Fe. Internal energy calibration was performed by the simultaneous measurement of absorption of the corresponding metal foil placed between two ionization chambers located after the sample. The first inflection point of the foil spectrum was assigned to 8980.3 eV for Cu and 7111.2 eV for Fe. To reduce photoreduction, data were collected on four distinct and physically separate spots, two spots for Cu and two spots for Fe. Totals of 12 and 19 scans were measured at the Cu and Fe K-edge, respectively, with no significant change from photoreduction observed.

XAS Data Analysis. The energy-calibrated averaged data were processed by fitting a second-order polynomial to the pre-edge region and subtracting this from the entire spectrum as a background. A three-region spline of orders 2, 3, and 3 was used to model the smoothly decaying postedge region. The data were normalized by scaling of the spline function to an edge jump of 1.0 at 9000 eV for Cu and 7130 for Fe. This background subtraction and normalization was done using *PySpline*.[92] The least-squares fitting program *OPT* in *EXAFSPAK*[93] was used to fit the data. Initial ab initio theoretical phase and amplitude functions were generated in *FEFF 7.0*[94] using crystallographic parameters of the oxo complex $[(F_8)FeOCu(AN)]^+$ as the starting model. The final model used was based on the DFT-optimized structure. Atomic coordinates were further adjusted as necessary as fits were improved. During the fitting process, the bond distance (R), and the mean-square thermal and static deviation in $R(\sigma^2)$ were varied for all components. The threshold energy (ΔE_0) was also allowed to vary for each fit but was constrained to the same value for all components in a given fit. Coordination numbers (N) were systematically varied to provide the best chemically viable agreement to the EXAFS data and FT but was fixed within a given fit.

rR Spectroscopy. Samples were prepared as previously described as 1 mM THF solutions in NMR tubes. Samples were excited at 413 nm using a Coherent I90C-K Kr^+ ion laser, while the sample was immersed in a liquid-nitrogen-cooled (77 K) EPR finger Dewar (Wilmad). The power was 2 mW at the sample. Data were recorded while rotating the sample to minimize photodecomposition.

(92) Tenderholt, A.; Hedman, B.; Hodgson, K. O. PySpline; Stanford Synchrotron Radiation Laboratory: Stanford, CA, 2006.
(93) George, G. N. *EXAFSPAK*; Stanford Synchrotron Radiation Laboratory: Stanford, CA, 2000.
(94) Rehr, J. J.; Albers, R. C. *Rev. Mod. Phys.* **2000**, *72*, 621–654.

The spectra were recorded using a Spex 1877 CP triple monochromator with a 1200 grooves/mm holographic spectrograph grating and an Andor Newton CCD cooled to −80 °C. Spectra were calibrated to toluene.

Computational Methods. DFT calculations were performed using *Gaussian 03*.[95] Models of **1** and **2** were constructed based loosely on crystallographically derived parameters of the monometallic molecular fragments. Calculations were performed with the BP86 functional within the unrestricted formalism [B3LYP incorrectly predicts the ground state as HS ($S = 3$), and a previous assessment of functional dependence for the truncated $[(P)FeOCu(AN)]^+$ complex supports the choice of the BP86 functional]. A triple-ζ basis set with polarization (6-311G*) was used on Cu, Fe, and O_2. A split-valence basis (6-31G) was used on all remaining atoms (F, C, and H), supplemented by polarization functions in the case of N (6-31 g*). Density fitting was employed and models were optimized to default convergence criteria (unless otherwise noted) on ultrafine integration grids. Models were first subjected to a coarse optimization on the HS ($S_T = 3$) surface, followed by a single-point calculation to obtain a spin-polarized broken-symmetry solution. The models were then reoptimized on the BS ($S_T = 2$) surface to yield final atomic coordinates. Analytical frequency calculations were performed to ensure that the stationary points on the models' respective potential energy surfaces had been reached. No imaginary frequencies were obtained. Mulliken population analysis was performed with *QMForge*.[96]

Generation of $[(F_8)Fe(O^{2-})Cu(AN)]^+$ $BArF^-$ (2a). In a 100 mL Schlenk flask equipped with a stir bar were placed, in the drybox, 210 mg (0.2 mmol) of $(F_8)Fe^{II}$ and 186 mg (0.2 mmol, 1.0 equiv) of $[(AN)Cu^I](BArF)$, to which was added air-free freshly distilled THF (20 mL). The reaction mixture was cooled to −80 °C (dry ice−acetone bath) and stirred for 30 min. The solution was subject to O_2 purging and finally allowed to warm slowly at room temperature and then layered with 50 mL of deoxygenated heptane. After 12 h, the solution was filtered and the black microcrystalline solid dried in vacuo (245 mg, 70% yield). Anal. Calcd (found): C, 53.28 (53.22); H, 2.58 (2.59); N, 5.58 (5.63). ^{1}H NMR (CD_2Cl_2): δ (s, 8H, pyrrole), 9.8−9.14 (d, 8H, *m*-phenyl), 7.67−7.51 (m, 16H, 8H, BArF + *p*-phenyl). UV−vis (CH_2Cl_2): 440, 557 nm.

Generation and Characterization of $[(DCHIm)(F_8)Fe^{III}(O_2^{2-})Cu^{II}(AN)]^+$ (2b). a. UV−Vis Spectroscopy. $[(F_8)Fe^{III}(O_2^{2-})Cu^{II}(AN)]^+$ (**2**) was synthesized as previously reported.[37] To 4 mL of a 0.36 mM THF solution of the O_2 adduct (**2**) was added 1.0 equiv (100 μL of 14.4 mM, 0.30 mg) of DCHIm to generate LS $[(DCHIm)(F_8)Fe^{III}(O_2^{2-})Cu^{II}(AN)]^+$, which was characterized by UV−vis spectra [λ_{max} (ε, mM^{-1} cm^{-1}) = 421 (Soret: 146.5), 537 (8.2) nm]. Warming of the solution leads to the formation of the hydroxo complex $[(F_8)Fe^{III}OH]$ with λ_{max} (ε, mM^{-1} cm^{-1}) at 412 (156.3) and 572 nm (9.3).

b. ^{2}H NMR Spectroscopy. In the glovebox, a 1:1 mixture of $(F_8\text{-}d^8)Fe^{II}\cdot H_2O$ (3.0 mg, 3.5 mM) and $[Cu^I(AN)]^+$ (3.32 mg, 3.5 mM) was taken in a 5 mm NMR tube and dissolved in 0.5 mL of THF. To the cold THF solution (at −80 °C, dry ice−acetone) of $(F_8\text{-}d^8)Fe^{II}\cdot H_2O$ and $[Cu^I(AN)]^+$ was bubbled in 2 mL of O_2, and the NMR was recorded at −80 °C. A peak at 96 ppm observed as reported previously corresponds to the chemical shift of pyrrole D atoms of $[(F_8\text{-}d^8)Fe^{III}(O_2^{2-})Cu^{II}(AN)]^+$. To the same NMR tube was added 1.5 equiv (1.2 mg of DCHIm in 0.05 mL of THF) of DCHIm, and a new peak at upfield 8.31 ppm was observed.

UV−Vis Spectroscopy Monitoring of the Reaction of $[(F_8)Fe^{III}(O_2^{2-})Cu^{II}(TMPA)]^+$ (1) with Axial Ligand Bases. In a modified low-temperature cuvette assembly equipped with a Schlenk-type side arm, a solution of **1** was generated in CH_3CN at − 40 °C, as previously described.[37] A stock solution of equimolar amounts of $(F_8)Fe^{II}\cdot H_2O$ (13 mg) and $[Cu^I(TMPA)(CH_3CN)](ClO_4)$ (8 mg) in 6 g of deoxygenated CH_3CN is prepared in a glovebox, and 0.3 g of a stock solution is diluted to 10 g and transferred to the UV−vis cuvette. Generation of the peroxo adduct [λ_{max} = 558, 535 (sh) nm] is accomplished by the bubbling of excess O_2 into the solution at −40 °C. The removal of excess O_2 is performed by the application of 3−5 vacuum/Ar cycles. Then 1, 3, and 5 equiv of 4-(dimethylamino)pyridine (DMAP) (50, 150, and 250 μL, respectively, of a DMAP stock solution prepared with 19.5 mg of DMAP in 10 mL of CH_3CN) were added and the respective spectra recorded at −40 °C (see Figure S2 in the Supporting Information). The new Q-band spectral feature (λ_{max} = 527 nm) is assigned to the formation of $(F_8)Fe^{II}(DMAP)_2$. A control experiment by the addition of DMAP to a solution of the mixture of $(F_8)Fe^{II}$/$[Cu^I(TMPA)(CH_3CN]^+$ yielded the same spectrum. The experiment was repeated in the nonpolar solvent CH_2Cl_2 (instead of CH_3CN) and also using 1,5-(dicyclohexyl)imidazole (DCHIm) as the axial ligand base (instead of DMAP) in CH_3CN, and the results were essentially the same in both cases.

Reaction of 1 with DMAP: Determination of O_2 Evolution. O_2 evolution was quantitatively determined using an alkaline pyrogallol solution (1,2,3-trihydroxybenzene), following a methodology used frequently in our laboratory.[29,37] In the glovebox, equimolar amounts of $(F_8)Fe^{II}\cdot H_2O$ (40 mg) and $[Cu^I(TMPA)(CH_3CN)](ClO_4)$ (24 mg) were dissolved in 10 mL of deoxygenated CH_3CN, transferred to a 50 mL Schlenk flask with a stirbar, and capped with a rubber septum. The flask was taken out of the glovebox, the solution was cooled down to −40 °C (by adding dry ice to the acetone bath and following the temperature by a thermocouple), and then O_2 was gently bubbled into the solution using a syringe with a long needle. To ensure complete formation of the peroxo compound, the solution was allowed to stand in the cold bath for 30 min. Excess/free O_2 wass removed via five freeze/pump/thaw cycles. In parallel with the reaction, 4.0 g of pyrogallol was dissolved in 25 mL of a deoxygenated 50% KOH solution in a specially designed 100 mL Schlenk flask possessing a 2-mm-path-length cuvette; its UV−vis spectrum was recorded. Excess DMAP (10 equiv: 1 mL solution prepared with 293 mg of DMAP in 5 mL of CH_3CN) was added to the peroxo adduct solution, thus allowing O_2 release. O_2 was then moved from the reaction flask to the pyrogallol flask by slowly passing argon through the headspace of the reaction flask and thus moving the O_2 through a cannula to the pyrogallol flask. O_2 was then bubbled directly into the pyrogallol solution, whose color changed from faint beige to dark brown after several minutes. After 20−30 min, the pyrogallol solution ceased becoming darker and its UV−vis spectrum was recorded. The amount of O_2 released was determined using a calibration curve in which absorbance (400 nm) = (0.0716 mL of O_2) + 0.025.[29] On the basis of the stoichiometry of the reaction where 1 equiv of the peroxo compound decomposes to give 1 equiv of O_2, two experiments yielded 90 and 91% O_2 detection.

(95) Gaussian 03, Revision C.02, Frisch, M. J.; Trucks, G. W.; Schlegel, H. B.; Scuseria, G. E.; Robb, M. A.; Cheeseman, J. R.; Montgomery, Jr., J. A.; Vreven, T.; Kudin, K. N.; Burant, J. C.; Millam, J. M.; Iyengar, S. S.; Tomasi, J.; Barone, V.; Mennucci, B.; Cossi, M.; Scalmani, G.; Rega, N.; Petersson, G. A.; Nakatsuji, H.; Hada, M.; Ehara, M.; Toyota, K.; Fukuda, R.; Hasegawa, J.; Ishida, M.; Nakajima, T.; Honda, Y.; Kitao, O.; Nakai, H.; Klene, M.; Li, X.; Knox, J. E.; Hratchian, H. P.; Cross, J. B.; Bakken, V.; Adamo, C.; Jaramillo, J.; Gomperts, R.; Stratmann, R. E.; Yazyev, O.; Austin, A. J.; Cammi, R.; Pomelli, C.; Ochterski, J. W.; Ayala, P. Y.; Morokuma, K.; Voth, G. A.; Salvador, P.; Dannenberg, J. J.; Zakrzewski, V. G.; Dapprich, S.; Daniels, A. D.; Strain, M. C.; Farkas, O.; Malick, D. K.; Rabuck, A. D.; Raghavachari, K.; Foresman, J. B.; Ortiz, J. V.; Cui, Q.; Baboul, A. G.; Clifford, S.; Cioslowski, J.; Stefanov, B. B.; Liu, G.; Liashenko, A.; Piskorz, P.; Komaromi, I.; Martin, R. L.; Fox, D. J.; Keith, T.; Al-Laham, M. A.; Peng, C. Y.; Nanayakkara, A.; Challacombe, M.; Gill, P. M. W.; Johnson, B.; Chen, W.; Wong, M. W.; Gonzalez, C.; and Pople, J. A.; Gaussian, Inc., Wallingford CT, 2004.

(96) Tenderholt, Adam L. QMForge, Version 2.1. Stanford University, Stanford, CA, USA.

Reaction of 1 with DMAP: Characterization of the Product $(F_8)Fe^{II}(DMAP)_2$. In the same experiment described above, $(F_8)Fe^{II}(DMAP)_2$ precipitated spontaneously and was isolated by filtration under argon, washed, vacuum-dried for 2 h, and finally stored in a glovebox. The yield was 70%. The purple solid was characterized by elemental analysis consistent with a formulation as a monohydrate solid, $(F_8)Fe^{II}(DMAP)_2 \cdot H_2O$, Desert Analytics, $C_{58}H_{42}N_8F_8FeO$ found/calcd: C, 64.5/64.8; H, 3.6/3.9; N, 10.1/10.4. UV−vis (CH_3CN, 293 K): λ_{max} 418.5 nm (Soret), 527 nm (Q band). ^1H NMR showing a typical spectrum of LS iron(II) porphyrin (400 MHz, CD_2Cl_2, 300 K): δ (ppm) 7.6 (pyrrole H), 7.2 (phenyl H), 1.5 (H_2O). The MALDI-TOF mass spectrum shows a peak characteristic of the monobase $(F_8)Fe^{II}(DMAP)$ (probably the other base is lost by the effect of the laser): m/z 935 ([M − DMAP − H_2O]), m/z 812 ([M − 2 DMAP − H_2O]).

UV−Vis Spectroscopy Monitoring of the Reaction of 2b with 2,4-Di-*tert*-butylphenol. In a UV−vis cuvette assembly, a solution of $[(DCHIm)(F_8)Fe^{III}(O_2^{2-})Cu^{II}(AN)]^+$ (0.36 mM) was generated in THF at −80 °C as described above; 1.0 equiv of 2,4-di-*tert*-butylphenol (0.29 mg, 14.4 mM) was then added. UV−vis absorption at λ_{max} (ε, $mM^{-1}\,cm^{-1}$) = 419 (Soret: 133.8) and 541 (8.5) nm corresponds to high-valent oxyferryl $[(DCHIm)(F_8)Fe^{IV}{=}O]$ (spectra are given in the Supporting Information, Figure S1).

Reactivity of 2b in the Presence of HCl and the Quantitive Determination of H_2O_2. Equimolar amounts of $(F_8)Fe^{II} \cdot H_2O$ (20 mg) and $[Cu^I(AN)(CH_3CN)]ClO_4$ (9.8 mg) were dissolved in 10 mL of CH_3CN (concn = 3 mM) in a glovebox. The solution was brought out of the glovebox and immersed in a cold bath at −40 °C, and O_2 was then bubbled through the solution to generate the HS peroxo compound **2a**. Excess O_2 was removed by several vacuum/Ar cycles; then 1.0 equiv of DCHIm (5.6 mg in 0.1 mL of CH_3CN) was added to form the LS peroxo complex **2b**. A total of 10 equiv of HCl (0.24 mL of a 1.0 M diethyl ether solution of HCl; Aldrich) was added, and the dark-red solution turned dark green. The solution was removed from the cold bath, followed by the addition of 20 mL of distilled water (final volume = 30.3 mL). A suspension is formed because of the insolubility of $(F_8)Fe^{III}Cl$ in the solvent mixture. H_2O_2 was determined spectrophotometrically (at 408 nm) upon the addition of 1 mL of a titanyl reagent [titanium(IV) oxysulfate in sulfuric acid, Riedel de Haën] to a 10 mL suspension, followed by centrifugation. A calibration curve was made in the same solvent mixture of the reaction (CH_3CN/ether/H_2O). The yield of H_2O_2 was determined to be 70% on the basis of two experiments.

UV−Vis Spectroscopy Monitoring of the Reaction of $[(DCHIm)(F_8)Fe^{IV}{=}O]$ (1c) with $[Cu^I(AN)][B(C_6F_5)_4]$. To the UV−vis cuvette containing a THF solution of $[(DCHIm)(F_8)Fe^{IV}{=}O]$ (prepared by the reaction of **2b** with 2,4-di-*tert*-butylphenol as discussed above) was added 1.0 equiv of $[Cu^I(AN)]^+$ (1.33 mg in 0.1 mL in THF) at − 80 °C. UV−vis absorption at λ_{max} = 440 and 553 nm corresponds to $[(F_8)Fe^{III}(O^{2-})Cu^{II}(AN)]^+$.

EPR Spectroscopy Identification of $[Cu^{II}(AN)(OH)]^+$ as the Product of the Reaction of 2b with 2,4-Di-*tert*-butylphenol. In a glovebox, 1.6 mg of $(F_8)Fe^{II} \cdot H_2O$ and 1.8 mg of $[Cu^I(AN)]^+$ were dissolved in 0.4 mL of deoxygenated acetone in a EPR tube. Outside the glovebox, the solution was cooled to −80 °C (acetone−dry ice bath) and bubbled with O_2 to generate the peroxo compound **2b**. A total of 1 equiv of DCHIm (50 μL of a 40 mM acetone solution of DCHIm) was added to the reaction mixture, followed by the addition of 50 μL of a 40 mM acetone solution of 2,4-di-*tert*-butylphenol (1 equiv). Then, the EPR spectrum was recorded at 77 K [EPR parameters $A_\parallel$ = 127.33 × 10^{-4} cm^{-1}, $A_\perp$ = 35 × 10^{-4} cm^{-1}, $g_\parallel$ = 2.24, and $g_\perp$ = 2.06]. The solution was warmed to room temperature, and again an EPR spectrum was recorded at 77 K. The thermally decomposed products $[(F_8)Fe^{III}OH]$ (g = 5.8) and $[Cu^{II}(AN)(OH)]^+$ were formed (spectra are given the Supporting Information, Figure S3).

Identification and Quantification of Coupled Phenol (3,3′,5,5′-Tetra-*tert*-butyl-(1,1′-biphenyl)-2,2′-diol) by GC−MS. In a glovebox, 16.6 mg of $(F_8)Fe^{II} \cdot H_2O$ and 18.5 mg of $[Cu^I(AN)]^+$ were dissolved in 2 mL of THF in a Schlenk flask. Outside the glovebox, the solution was cooled to −80 °C and bubbled with O_2 to generate the peroxo adduct. The excess O_2 was removed by employing a vacuum and Ar bubbling through the solution for two cycles. To the solution was added 4.6 mg of DCHIm in 0.2 mL of THF (1 equiv), followed by the addition 1 equiv of 2,4-di-*tert*-butylphenol (4.6 mg of phenol in 0.4 mL of THF). Then the solution was stirred for 2 h and warmed to room temperature. The volume of the solution was reduced to 0.5 mL, and the metal complexes were precipitated by the addition of 10 mL of pentane and separated by filtration. The filtrate was carefully collected, pentane was removed by a vacuum, and the organic residue was redissolved in 4 mL of CH_3CN. The coupled phenol generated in this reaction was quantitatively determined by GC−MS. The yield of 3,3′,5,5′-tetra-*tert*-butyl-(1,1′-biphenyl)-2,2′-diol was 68.5% (the GC−MS trace is given in the Supporting Information, Figure S4).

Identification of the 2,4,6-Tri-*tert*-butylphenoxy and 2,4-Di-*tert*-butyl-4-methoxylphenoxy Radicals by EPR Spectroscopy. This reaction was carried out in a manner similar to that described above except that either 2,4,6-tri-*tert*-butylphenol or 2,4-di-*tert*-butyl-4-methoxylphenol was used. Then, the EPR spectrum was recorded at 77 K; the g values for the 2,4,6-tri-*tert*-butylphenoxy and 2,4-di-*tert*-butyl-4-methoxylphenoxy radicals are 2.0056 and 2.0077, respectively.

Acknowledgment. These studies were supported, in part, by the National Institutes of Health (NIH; Grant DK031450 to E.I.S. and Grant RR-001208 to K.O.H.). Computational resources used in these studies were provided, in part, by the Bioinformatics Center of the University of Arkansas for Medical Sciences [NIH P20 RR-16460 from the IDeA Networks of Biomedical Research Excellence Program of the National Center for Research Resources (NCRR)] and, in part, by the National Science Foundation through TeraGrid resources provided by the NCSA (Grant TG-CHE080054N). K.D.K. acknowledges support from the NIH (Grant GM60353) and WCU Program R31-2008-000-10010-0. The XAS data were measured at SSRL, the operations of which are funded by the Department of Energy, Office of Basic Energy Sciences. The SSRL Structural Molecular Biology program is supported by the National Institutes of Health, NCRR, Biomedical Technology Program, and by the Department of Energy, Office of Biological and Environmental Research. This publication was made possible by Grant 5 P41 RR001209 from the NCRR, a component of the NIH. Its contents are solely the responsibility of the authors and do not necessarily represent the official view of NCRR or NIH.

Supporting Information Available: UV−vis spectra of the reaction of **2b** with 1 equiv of 2,4-di-*tert*-butylphenol (Figure S1), UV−vis spectra of the reaction of **1** with DMAP (Figure S2), EPR spectra of the reaction of **2b** with 1 equiv of 2,4-di-*tert*-butylphenol (Figure S3), GC−MS trace of the oxidative coupling of 2,4-di-*tert*-butylphenol in the presence of **2b** (Figure S4), ORTEP diagram (Figure S5), crystal data and structure refinement for the **2a** X-ray structure (Table S1), XAS spectra (Figures S6−S9), computational data (Tables S2−S8), and crystallographic data in CIF format. This material is available free of charge via the Internet at http://pubs.acs.org.